

Inside the cocoon: a comprehensive explanation of the spectra of Little Red Dots

A. Sneppen^{1,2*}, D. Watson^{1,2}, J. H. Matthews³, G. Nikopoulos^{1,2},
 N. Allen^{1,2}, G. Brammer^{1,2}, R. Damgaard^{1,2}, K. E. Heintz^{1,2}, C. Knigge⁴,
 K. S. Long^{5,6}, V. Rusakov⁷, S. A. Sim⁸, J. Witstok^{1,2}

¹Cosmic Dawn Center (DAWN)

²Niels Bohr Institute, University of Copenhagen, Blegdamsvej 17, København 2100, Denmark

³Astrophysics, Department of Physics, University of Oxford, Oxford OX1 3RH, UK

⁴School of Physics and Astronomy, University of Southampton, Southampton SO17 1BJ, UK

⁵Space Telescope Science Institute, 3700 San Martin Drive, Baltimore, MD 21218, USA

⁶Eureka Scientific Inc., 2542 Delmar Avenue, Suite 100, Oakland, CA 94602-3017, USA

⁷Jodrell Bank Centre for Astrophysics, University of Manchester, Oxford Road, Manchester M13 9PL, UK

⁸Astrophysics Research Centre, The Queen’s University of Belfast, University Road, Belfast, BT71NN, United Kingdom

* Corresponding Author: Albert Sneppen (a.sneppen@gmail.com)

JWST has revealed a population of compact galaxies in the early Universe with broad emission lines and strong Balmer breaks; among them the so-called “little red dots” (LRDs). Their nature remains uncertain with hypotheses including exotic phenomena. We assemble a sample of LRD-like objects at $z > 3$ and use self-consistent radiative-transfer calculations to show that a supermassive black hole accreting from a dense gas cocoon accurately reproduces the detailed spectra. We show that the cocoons must be non-spherical, with comparable amounts of inflowing and outflowing material. And we predict correlations between Balmer break strength, Balmer line-absorption and scattering line width, which we confirm in our observed sample. We reproduce all LRD-like properties without requiring star-like atmospheres and we determine the typical black hole in our sample to be of order a million solar masses, with ionized cocoon masses of tens of solar masses potentially supplied from a much larger cold-gas reservoir.

1 Introduction

Little Red Dots (LRDs) are a population of luminous high-redshift sources recently identified by *JWST* (1–4), which exhibit an unusual combination of properties: i) they are spatially unresolved with *JWST* at least in the red part of the spectrum, implying sizes $\lesssim 100$ pc (5, 6) or even (7); ii) they have ‘v-shaped’ continua with a blue UV-slope and a sudden change of slope which occurs close to the Balmer break (8, 9); iii) they display broad hydrogen and helium emission lines with widths of a few thousand km s^{-1} (3, 4, 10), iv) with predominantly exponential line shapes (11); and v) they have relatively narrow red- and blueshifted H I Balmer and He I absorption, including possible P Cygni and inverse P Cygni features (11, 12). LRDs are a subset of a broader set of objects with the same compactness, broad recombination lines and Balmer breaks, but with somewhat different colour properties to LRDs, that all appear to have optical spectra dominated by ionized gas emission (11, 13–15). We refer to this more general set as ‘LRD-like’ objects. No model so far proposed has quantitatively and self-consistently explained all of their major features (13, 16–21). The most favoured concept currently involves an accreting supermassive black hole (SMBH) due to their extreme compactness (22), broad H and He emission lines (23, 24), and extreme luminosities in small inferred volumes (11). However, beyond the difficulty of explaining the strong Balmer breaks and Balmer absorption lines and exponential line-shapes, typical active galactic nuclei (AGN) indicators such as X-ray (25–27), radio (9, 28, 29), and infrared excess (30, 31) emission are generally not detected, and only limited long-term variability has been found (32–36). In addition, SMBH masses based on single epoch virial methods are orders of magnitude ‘overmassive’ (37) relative to their host galaxies (10, 23, 38–41).

However, modelling LRD-like objects as rapidly accreting SMBHs embedded in dense, ionized gas (11, 13, 14, 42) seems able to resolve some of these issues. First, the exponential form of the broad line wings, e.g. ref. (24, 43) indicates that the broadening is dominated by high column density electron scattering rather than Doppler motions (11), implying smaller black hole masses (, see also ref. (44)). Second, such high columns could naturally give rise to the deep Balmer breaks and the Balmer and He I line absorption (4, 6, 11, 13, 14, 45), and deviations from Case B line ratios (46, 47). Both radio and X-ray emission could also be suppressed in this scenario, see ref. (11, 27, 48). Initial theoretical investigations are emerging (11–14). However, to robustly infer the physics of LRDs, we need to include all of these effects. We therefore present here the first self-consistent, quantitative model of LRD-like objects, which can simultaneously reproduce the various observed properties.

In this work, we present a spectroscopic sample of high signal-to-noise ratio (SNR) Balmer-break plus broad-line objects above $z = 3$ observed with *JWST* (Sect. 2) and use that sample to compare to our self-consistent Monte Carlo ionisation and radiative transfer simulations (Sect. 3) showing that the models reproduce very well the properties of the objects in the sample. The surprising effectiveness of our first-principles modelling framework provides fundamental new insights into, and powerful diagnostics of, the LRD phenomenon, which we outline in Sect. 4. We also then create models for several well-studied LRDs with extreme properties to

demonstrate the power and completeness of the framework.

2 Observations

We first found objects at redshift $z > 3$ with median $\text{SNR} > 2.5$ per pixel in NIRSpec/PRISM in the DAWN *JWST* Archive (DJA) (49, 50). Below this redshift the number of LRDs decreases rapidly as non-LRD interlopers increase. Selection was then based on i) a strong Balmer break: $D_{4000} = F_{4200\text{\AA}}/F_{3500\text{\AA}} > 1.2$ in the *JWST* NIRSpec/PRISM, following the definition of ref. (51) and ii) a broad $\text{H}\alpha$ line as detected in the medium- or high-resolution ($R \sim 1000\text{--}3000$) grating. We also included objects with grating spectra with a median $\text{SNR} > 5$ per pixel over $\text{H}\alpha$ and evidence for a Balmer break in photometry (i.e. without PRISM data, see App. A). These criteria yielded thirty objects at $z = 3.1\text{--}7.0$. The sample does not include the Rosetta Stone object (48), as it is below the redshift cut-off, or MoM-BH*-1 (14), as it does not have a grating observation that covers $\text{H}\alpha$, but we still make quantitative predictions using Sirocco for these extreme LRD objects.

The colour properties of the sample are illustrated in Fig. 1. Although the colour selection only restricts the Balmer break, 70% of objects have a v-shaped SED in the UV-optical, despite no UV colour selection being imposed. Further, while no morphological information is included in the selection, the sources typically appear unresolved, with PSF-corrected Sérsic radii $R_{50}(f_{F444W}) = 0.2_{-0.2}^{+0.7}$ kpc (median and 1σ distribution percentiles). Thus, these systems are compact and near the resolution limit in the red. On the other hand, a sizeable subset is spatially extended in the blue filters—e.g. 30% with $R_{50}(f_{F115W}) > 1$ kpc—typical of LRDs, e.g. ref. (52). We fit the $\text{H}\alpha$ lines in the grating spectra. Most objects favour an exponential line shape, with no object significantly favouring Gaussian broad lines (see App. A). The exponential line-profiles are typically symmetric (see, for example, Fig. 1, right panel), and always close to symmetric. The symmetry/asymmetry of the electron-scattered wings is an important diagnostic of the geometry of the system and we discuss this further below.

3 Methods

To model the gas behaviour and emitted spectra, we use the open-source Monte Carlo code, *Simulating Ionisation and Radiation in Outflows Created by Compact Objects* (Sirocco) (53, 54). While important radiative transfer studies of LRDs (13, 35, 55) have been performed using the Cloudy code (56), this does not self-consistently model electron-scattering redistribution of line photons and is limited to a one-dimensional geometry. We adopt Sirocco because its Monte Carlo radiative transfer framework is specifically designed to treat optically thick, multi-dimensional flows and includes Compton scattering and relativistic effects. Sirocco self-consistently computes the cocoon’s ionisation structure and radiation field(57), setting the electron column density, the strengths and linewidths of the recombination emission, the extent of partially ionised material and the strength of Balmer and Paschen absorption lines and break.

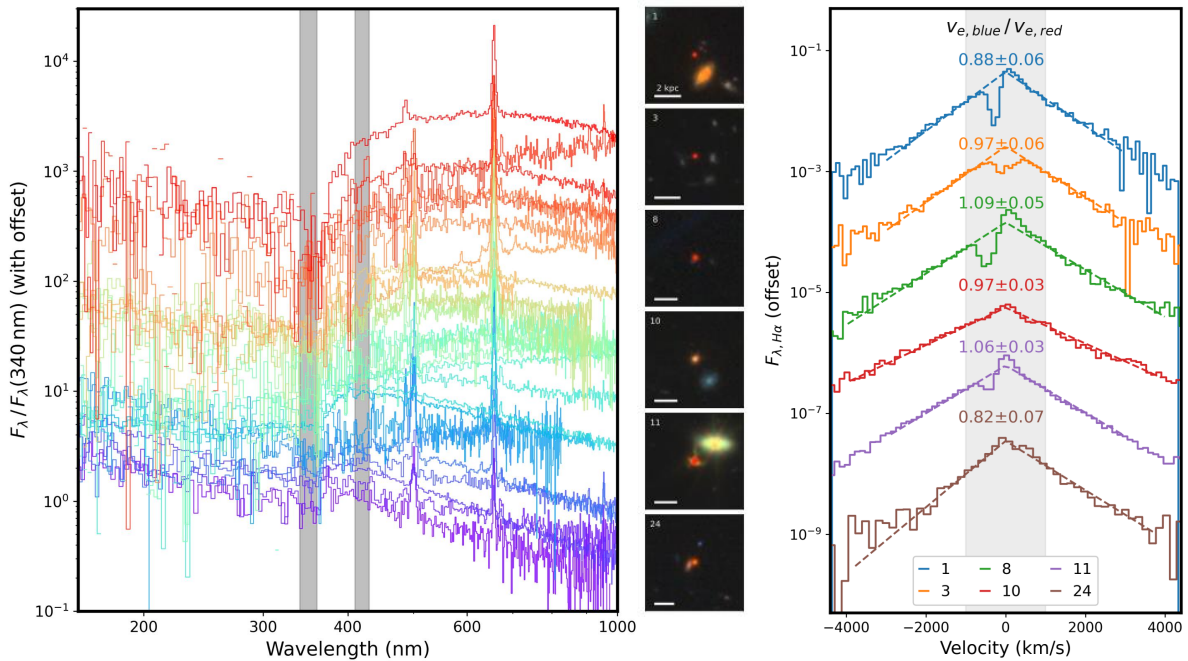


Figure 1: Properties of the LRD sample ($3.1 < z < 7$). *Left:* JWST NIRSpec/PRISM spectra highlighting the Balmer break and the ‘v-shape’ SED. *Middle:* JWST imaging of a subset of the sample showing the compact nature of the sources (see imaging information for the full sample in App. A). *Right:* Observed H α lines on a semi-logarithmic plot showing the exponential wings (a straight line on this plot) and the red/blue symmetry of the lines. The ratio of the exponential slopes on the blue and red sides, $v_{e,\text{blue}}/v_{e,\text{red}}$, is indicated over each line, showing a high degree of symmetry; we note a $> 2\sigma$ asymmetry in the bottom object, ID 24 (‘the Cliff’).

SIROCCO thus permits the quantification of different spectral properties, such as the correlation between the Balmer break strength and Balmer line widths. Further details on parameters and code assumptions can be found in App. B and (54).

Our basic theoretical framework consists of an accreting SMBH, ionising gas in a cocoon around it. The cocoon is axisymmetric with rotational Keplerian support around the SMBH and parameterized inflow and outflow kinematics (homologous, β -law winds or multiple angular components). The lack of spherical symmetry in the gas flow is demanded by the observations, as explained below. The ionisation and excitation structure of LRDs then emerges naturally from this framework, as shown in Fig. 2. A quasi-spherical Strömgren sphere of ionised gas is produced by the ionising radiation from the central source. This ionised gas is the first region of reprocessing with a very high column density, electron-scattering medium. Further out, a partially ionised layer with a substantial population of hydrogen in $n = 2$ is formed, causing bound-free absorption opacity which gives rise to the observed Balmer absorption lines and breaks. The effect of these layers can be seen by looking at how the local radiation field propagates through the gas cocoon (Fig. 2, lower right). Previous semi-analytic (11, 58) and radiative transfer studies (11, 12) assumed a static electron-gas for AGNs and LRDs, but by including bulk velocities we can test for absorption kinematics and diagnose scattering-wing asymmetries induced by bulk motion (App. C). Observationally, Balmer and He I absorption features have velocities in the range approximately -400 to $+100$ km/s, indicating both inflowing and outflowing gas in different objects, with the preponderance outflowing. The relative symmetry of the electron scattering wings in most objects, however, supports a net gas flow close to zero, i.e. an approximate balance between inflow and outflow, as discussed further in §4.3. This is the reason we must sacrifice spherical symmetry in our framework and move to an axisymmetric model. The diversity of our LRDs and LRD-like objects can be modelled with accreting black holes with luminosities (10^{43} – 10^{45} erg s $^{-1}$) and a surrounding cocoon of densities 10^6 – 10^{10} cm $^{-3}$, initialized between $R = 10^{15}$ – 10^{18} cm with a falling radial density profile, fiducially $\rho \propto r^{-2}$. The values are suggested in ref (11) based on the width of the H α scattering wings and absence of scattering in the [OIII] lines. We also explore the gas metallicity from [M/H] ~ -3 up to 0 to capture the impact of cooling efficiency on the shape of the electron-scattering wings.

4 Reproducing LRD spectral properties

In Fig. 3, we show a comparison of our observed sample with synthetic spectra from our models. The model spectra reproduce the hallmark LRD features. i) A Balmer break, arising from bound-free absorption in dense, partially neutral gas (8) – i.e. a non-stellar origin for the break, consistent with previous 1D photoionisation modelling (59). ii) Broadened hydrogen and helium recombination lines with exponential-shaped wings (11, 43). The diversity in Balmer break strengths and FWHM exponential widths are a natural consequence of SMBHs embedded in gas cocoons over a range of densities. iii) Blueshifted Balmer absorption lines, due to the outflows,

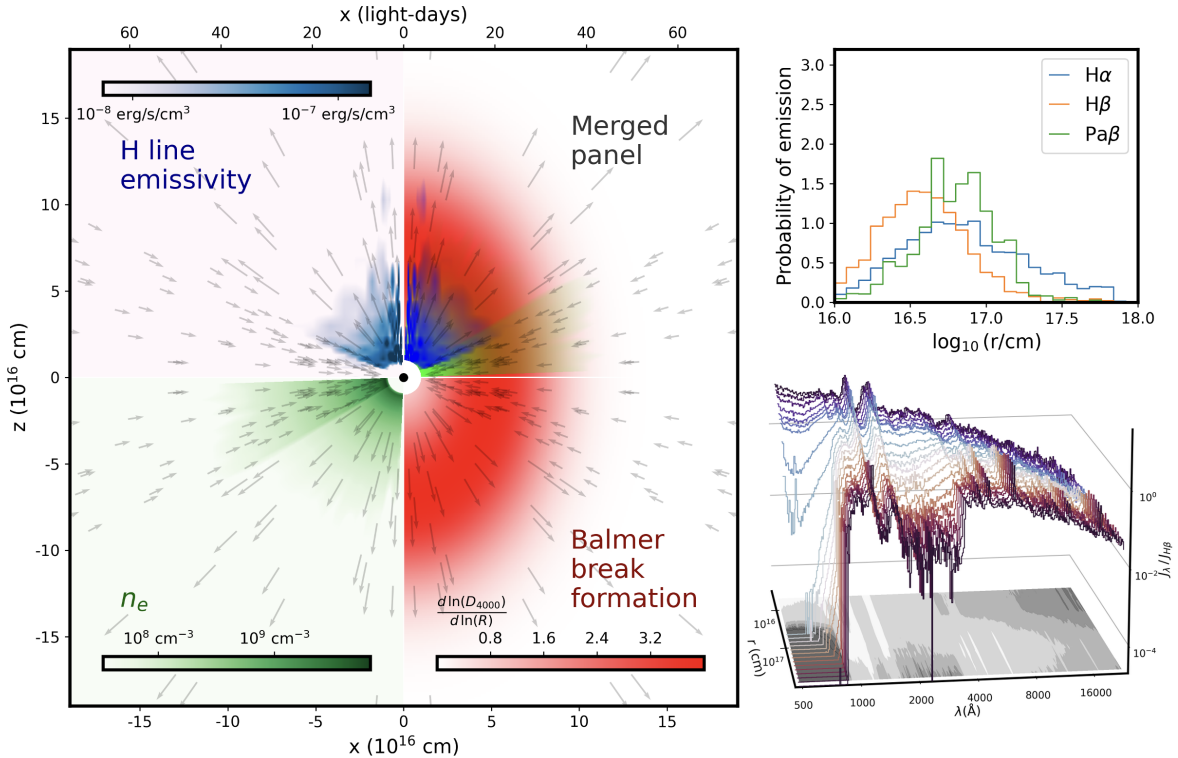


Figure 2: Overview of the physical structure of an LRD-like object, showing the gas flows and the spectral-formation regions in the ionised gas cocoon surrounding the central SMBH. *Left:* Inputs to the model are represented by the vector field, with arrows denoting the velocity (arrow length) and density (arrow density) of the gas. The data require both inflow and outflow (see Fig. 5 and §4.3). Outputs of the model are shown in the different quadrants: colours indicate the regions producing the Balmer break (red/orange), the electron density (green), and the hydrogen-line emissivity (sum of Balmer and Paschen lines, blue). *Top right:* radial distributions for the emission of escaped photons in H α (blue), H β (orange), and Pa β (green). The different recombination lines are not released from identical radii. *Bottom right:* the local monochromatic mean intensity at various radii through the cocoon (with a greyscale contour plot showing the projection). This illustrates that recombination lines form in the inner ionised gas, whereas the Balmer break is formed further out, where a sufficiently large $n = 2$ population is present.

where the absorption can be deep enough to remove flux both from the emission line and from the underlying continuum. iv) A broad range of SED shapes, with breaks close to the Balmer limit formed by the combination of Balmer breaks and a transmitted fraction of the incident blue spectrum. In terms of their spatial appearance, they would appear compact, with emission blueward of the Balmer break likely dominated by host galaxy emission. The addition of a star-forming host galaxy component in the UV would add an even greater range of SED shapes, though we do not model the host galaxy component here. These objects would generally still have a break at Balmer wavelengths, however, where the AGN is luminous. The sources could therefore appear spatially extended at UV wavelengths, while appearing compact in the red. In addition, a more detailed look at any given model spectrum (see Fig. B1) also shows mild differences in shapes between different Balmer lines due to resonant scattering and losses to bound-free absorption, which produce heterogeneous line profiles for different transitions. This is contrary to the first-order assumption which would produce similar width lines due to the near-constant Thomson-scattering cross-section with wavelength (60). Absorption lines from Ca II are also produced, as observed in low-redshift analogs of LRDs (61).

4.1 Physical parameters and predictions of the models

Significant electron-scattering wings require a lower column density of ionised material ($N_e \gtrsim 10^{24} \text{ cm}^{-2}$), compared to the columns needed for absorption in Balmer lines and Balmer breaks (e.g. $N_H \gtrsim 10^{25} \text{ cm}^{-2}$ for $n_H = 10^{10} \text{ cm}^{-3}$). The magnitude of the Balmer break is sensitive to both the gas density and the total column (n_H and N_H), whereas the electron-scattering wings depend mainly on the ionised column density and electron temperature, and the strength of the recombination lines depends on the total ionised mass and the density. These observables are therefore complementary in the information they provide. One example is the relation between H α line width and Balmer break strength; our models predict a correlation up to moderate column densities (Fig. 4). However, the scattering width does not exceed $\sim 3000 \text{ km/s}$ because as photons are scattered more often, they are increasingly absorbed before they can escape. Observationally, we see this prediction fulfilled in the sample data where there is a clear correlation up to a Balmer break strength of about 2, and no object in the sample is broader than 3000 km/s. A corollary is that objects with very extreme Balmer breaks should exhibit comparatively weaker and narrower recombination lines. We see this phenomenon in ‘The Cliff’ and ‘MoM-BH*-1’ objects that have exceptionally strong breaks, but relatively weak and narrow lines (see Fig. 6). A generic feature of the model spectra is a correlation between the emission line strengths and the continua, since they are both created by recombination, i.e. the hydrogen-line *equivalent widths* are similar across objects. In other words, the Balmer-line luminosities closely track the Paschen recombination continuum (see Fig. B6). This is an observational trend noted in the LRD sample of ref. (42), while it emerges naturally in our simulations because both the lines and the continuum are produced self-consistently by reprocessing of the same UV emission. Lastly, the SIROCCO models predict that Balmer line-absorption strengthens with Balmer-break prominence; this trend is also present in the observational sample (Pearson test, $p = 0.04$).

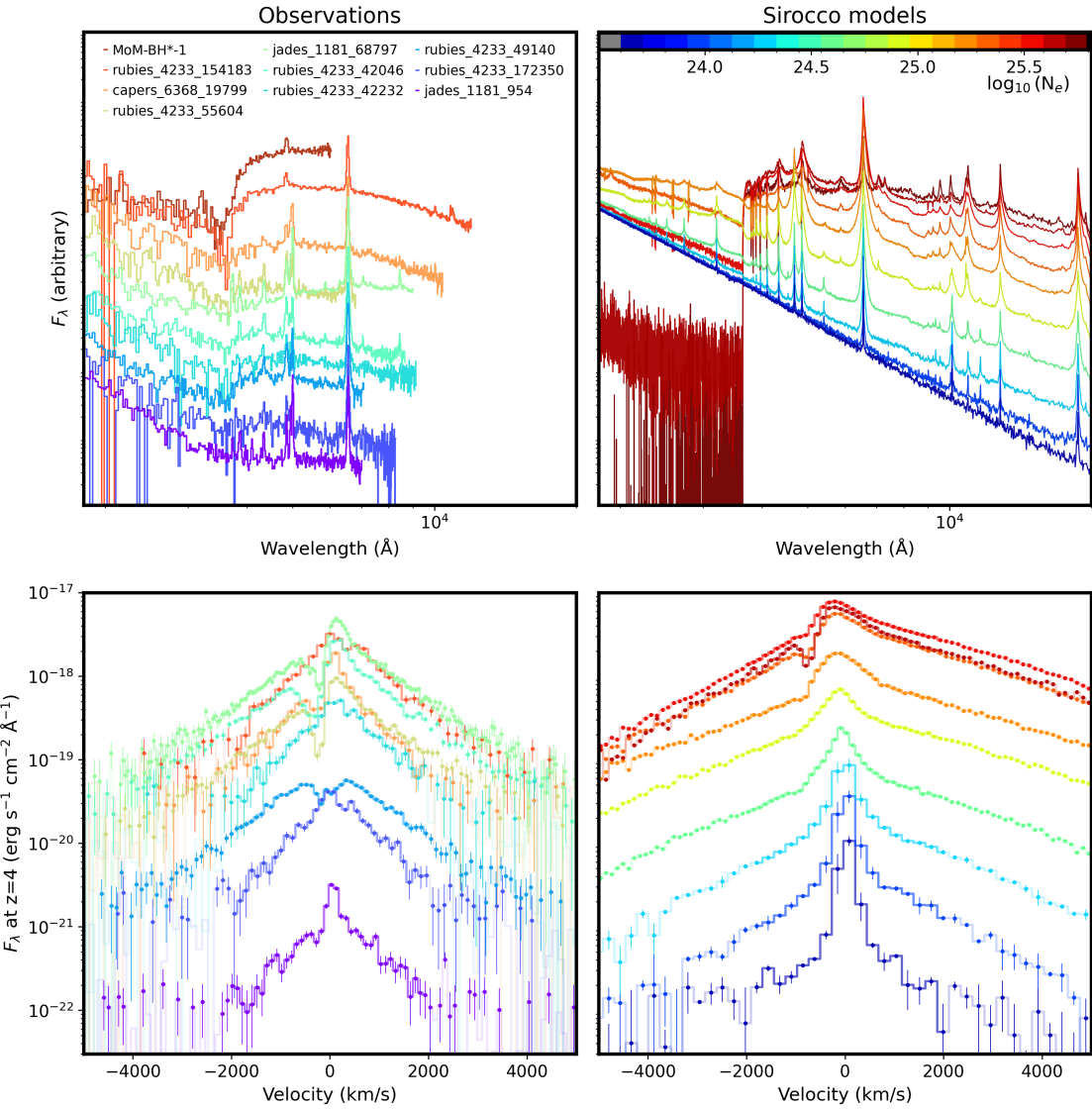


Figure 3: Comparison of the spectra and line shapes of observed LRD-like objects (left) and Sirocco models (right). The spectra are ordered by Balmer break strength, with the corresponding H α line profiles shown in the same ordering. *Top left:* Sequence of observed sources with increasingly prominent Balmer breaks. *Top right:* Spectra from a sequence of Sirocco models with varying column density in a homologous wind (keeping all other properties constant). Significant electron-scattering wings require a lower column density ($N_e \gtrsim 10^{24} \text{ cm}^{-2}$) compared to the Balmer breaks and absorption lines ($N_H \gtrsim 10^{25} \text{ cm}^{-2}$, (41)). *Bottom:* H α spectra from the same observational sample (left) and Sirocco density-sequence (right) scaled to the luminosity distance at $z = 4$. For both models and observations, the most luminous H α lines and the strongest Balmer break systems (i.e. the most massive cocoons) typically display broader wings and are more likely to have Balmer-absorption line profiles.

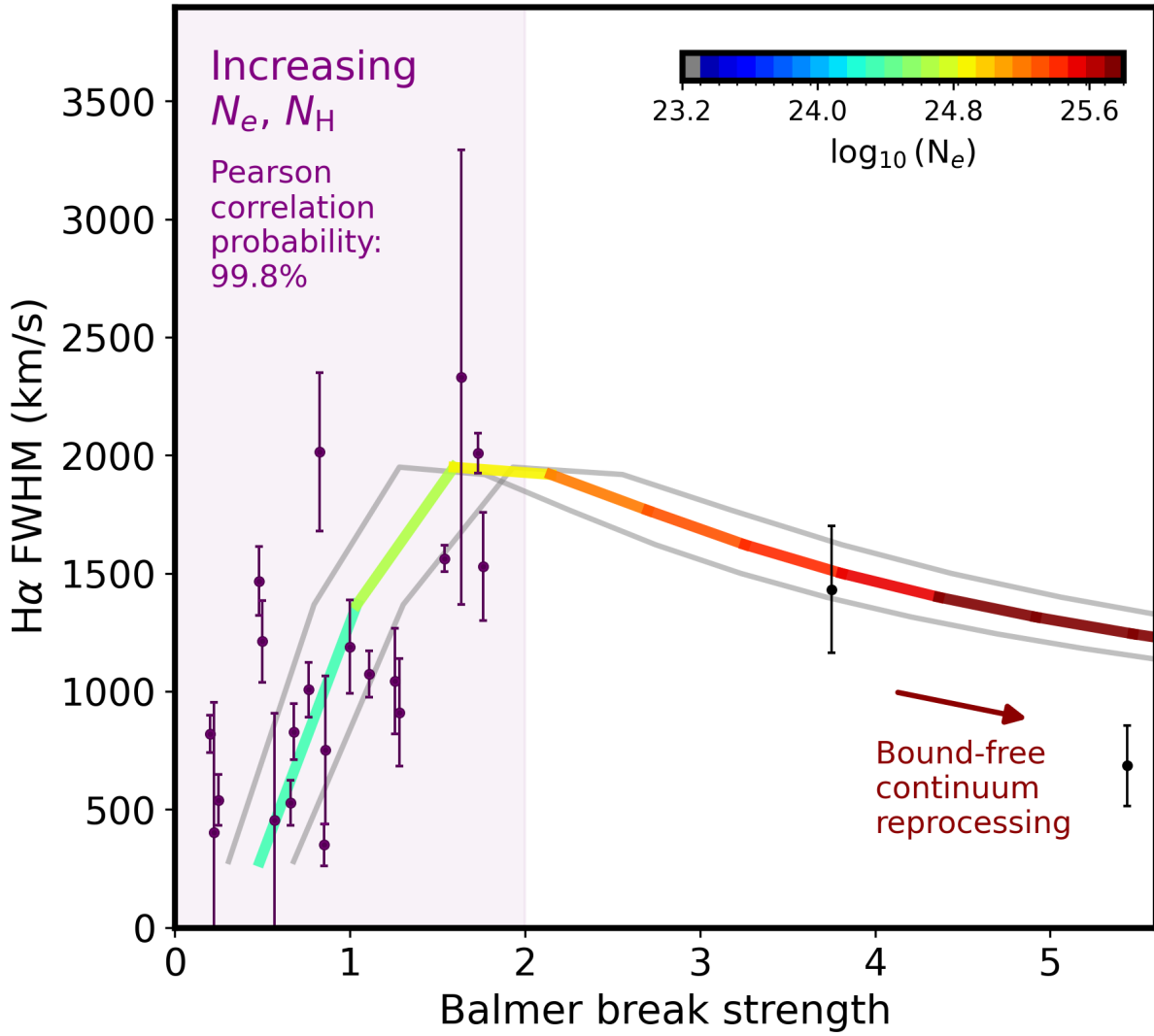


Figure 4: Comparison of the $H\alpha$ broad line width and the Balmer break strength for the observed sample. The curve shows an illustrative SIROCCO model density-sequence. To account for reddening, we apply a dust screen with $E(B - V) = 0.8 \pm 0.2$; the coloured curve shows the mean sequence, while the grey curves shift the models horizontally in Balmer-break strength by varying $E(B - V)$ within the quoted range. The initial positive correlation between line width and break strength arises because both the free-electron column density and the $n = 2$ population increase with total gas column density. At sufficiently large column densities, however, the extreme scattered wings (requiring multiple scatterings) are decreased due to continuum absorption opacity. The observed data appear to follow this predicted pattern.

4.2 The continuum shape, blackbody emission, and the black hole star

The transmitted UV flux and the Balmer break produce the characteristic LRD-like SED. However, this configuration only occurs over a narrow density range ($\lesssim 0.5$ dex) before the photons blueward of the Balmer break are very strongly suppressed (see Fig. 3). This is consistent with the LRDs, which are only compact in the reddest filters: once the AGN continuum collapses blueward of the break, stellar emission can easily dominate the observed UV light, and in most LRD-like objects, we do not anticipate strong UV flux transmitted directly from the accretion region, explaining the absence of extreme ionization signatures in their UV spectra (2).

Many of the concepts proposed to explain LRD-like objects involve a stellar-like atmosphere, e.g. black hole star (14), quasi-star (17), or supermassive stars (62), which might suggest a blackbody-like continuum emission. The rise redward of the Balmer break and the slope of the Paschen continuum emission may be reminiscent of blackbody emission, see ref. (42). But the red tail of emission in Sirocco is generally shallower than the Rayleigh-Jeans tail. In other words, the models are not optically thick and reprocessing to the maximum entropy distribution. Dust in cool gas outside the ionized cocoon or in the host galaxy can redden the spectrum further, providing a wider range of rest-NIR spectral slopes. We fit modified blackbodies to the Sirocco-model spectra in Fig. 3 including a modest level of extinction. We can fit the continua of the model spectra well with these modified blackbodies, as found in observations (42). Similar to these observational findings, the model spectra can be both narrower and broader than blackbodies (i.e. with blackbody β_{mbb} values between -4 and 3 , see Fig. B8), and we find only a weak correlation between the best-fit blackbody temperature and the luminosity. Such a weak correlation is reminiscent of a Hayashi-like track populated by LRDs and has direct relevance for the consideration of LRDs as a stellar-like object (13, 14, 42, 63). However, in the Sirocco models, there is no blackbody, and the weak correlation arises from the robust reprocessing to wavelengths longward of the Balmer break. Indeed, a simple blackbody framework does not predict a Paschen jump at around 820 nm, which can be produced in our model spectra, nor would it predict differences in the exponential widths of various hydrogen lines due to the wavelength-dependence of bound-free absorption opacity which are also predicted with Sirocco and observed (see Sect. 4.4). Further, a strong correlation exists between the Paschen continuum and $H\alpha$ emission both in our models across the parameter-space, and is independently observed in the data (42), see Fig. B6. This correlation exists because the line and continuum emission are both driven by the same hydrogen and helium recombinations. As recombination occurs inside any potential exterior reprocessing photosphere, in a blackbody model, $H\alpha$ emission would be suppressed in comparison to the continuum for a photosphere resulting from significant reprocessing. We conclude that the restframe optical and NIR continuum in LRDs therefore seems almost certain to be mostly Paschen and Brackett recombination emission. Opacity due to H^- is not currently included in Sirocco and may produce more blackbody-like spectral shapes. However, given how closely our models currently match the data, additional continuum opacity is unlikely to change our major conclusions.

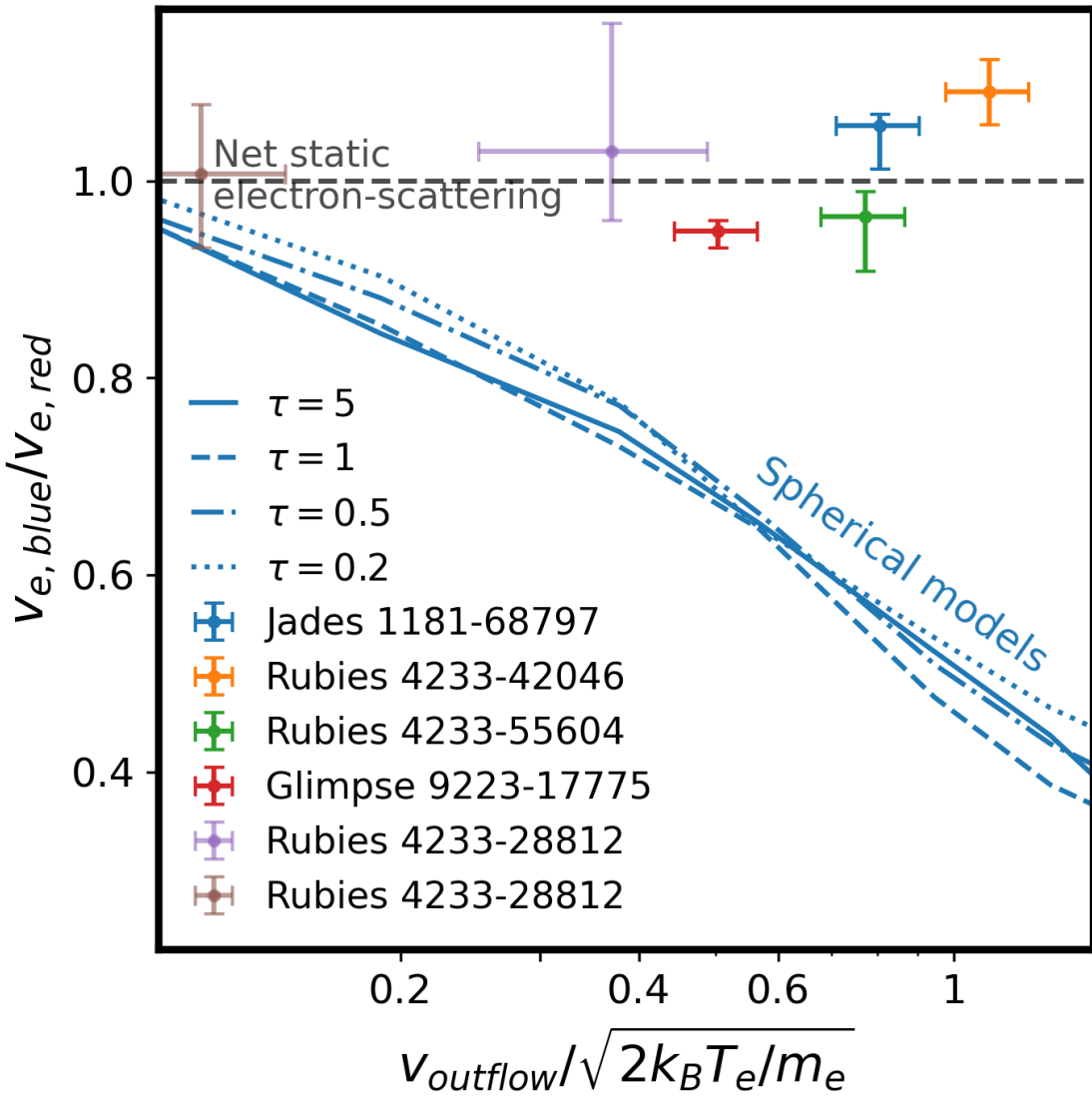


Figure 5: Symmetry of the H α scattering wings as a function of the outflow velocity. The blue curves show the line asymmetry predicted for spherical kinematics. Sample sources with significant blueshifts are plotted. All objects are strongly discrepant with a spherical outflow model, implying that both inflow and outflow must be present. The symmetry is measured by taking the ratio of the exponential slope on the blue side of the line to that on the red side. The outflow velocity is derived from the H α absorption line and is plotted in units of the thermal electron velocity. The models do not predict perfectly symmetric profiles, and indeed, several objects show small, but measurable asymmetry.

4.3 Non-spherical kinematics

As mentioned above, most LRD-like sources cannot be spherically symmetric in their kinematics. The reason for this is the following. A significant fraction have absorption lines with central velocity shifts of a few hundred km s^{-1} (10, 11), since most of these are blueshifted, this indicates a moderate velocity outflow. However, these velocities are comparable to the the thermal velocities of the electron gas at about 10 000 K. For a spherical outflow, this would result in highly asymmetric scattering wings in the emission lines (see App. C). The near-symmetry of the observed scattering wings indicates that the net flow is quite small ($\lesssim 100 \text{ km/s}$). So either the cocoons have a very slow outflow, which is contradicted by the observed absorption line velocities, or the mass outflow is approximately balanced by the mass inflow. To reconcile the observations we must therefore depart from a spherical kinematic geometry. In Fig. 5 we compare the line symmetry of the objects with blueshifted absorption lines to the results of spherical outflowing models as a function of outflow velocity. These observations show clearly that the cocoon cannot be spherically-symmetric in its velocity structure, else the scattering wings would be strongly asymmetric. This is why, as noted above, our Sirocco models therefore use axisymmetric geometries. The existence of an inflow and outflow clearly indicates that the objects are accreting from outside the ionized cocoon and feeding back most of the gas. The diversity of P Cygni profiles, as well as occasional inverse P Cygni and rest-wavelength absorption, then arise from viewing equatorial accretion inflows and polar feedback outflows at different inclination angles.

Such inflow/outflow is unlikely to be in perfect balance without fine-tuning, however, and we should expect to observe some degree of asymmetry in the lines. With sufficient quality data, it is clear that the scattered emission lines do indeed deviate slightly from perfect symmetry, at the level of a few percent (Fig. 5). For very large column densities (objects with large Balmer breaks), photons preferentially escape along the least obscured sightlines. The direction of the line asymmetry indicates whether the inflow or the outflow has the larger electron scattering optical depth. The Cliff LRD (6), with its extreme Balmer break, displays relatively large asymmetries. Allowing for a shift in the line center, it still displays a 2.8σ significance asymmetry of the wings of $\text{H}\alpha$ redward (see Fig. C2) indicating a higher optical depth in inflow than outflow, consistent with a higher velocity, lower density outflow compared to the inflow. The highest SNR $\text{H}\alpha$ lines in the sample are shown in Fig. A3, where dramatic improvements to the fitted model residual ($\Delta\text{BIC} > 40$) are attained by permitting a steeper exponential towards the blue than the red, once again pointing toward a lower-density outflow.

4.4 Differences in Balmer and Paschen line widths – deciphering the Rosetta Stone

A striking feature of both the model spectra and the observed LRDs is that the line widths, i.e. the slopes of the exponential line fits, differ for different hydrogen lines (see Fig. 6, bottom right). Naively, since Thomson scattering is largely wavelength-independent, the smaller

observed width of $\text{H}\alpha$ compared to $\text{H}\beta$ and $\text{Pa}\beta$ in the Rosetta Stone object, has been taken as evidence against electron scattering (48, 60). However, such differences are expected under bound-free absorption and electron scattering opacity. Fig. B7 shows a model spectrum with scattering widths in $\text{Pa}\beta$ and $\text{H}\beta$ 50–60% larger than in $\text{H}\alpha$; these are similar differences in velocity-width and the same hydrogen line ordering as seen in the Rosetta Stone (60). This is because a larger fraction of $\text{H}\alpha$ wing photons are lost to bound-free continuum opacity. For a more detailed explanation of this effect, see App. B.6.

The sequence of observed widths is not monotonic with wavelength, as would be expected if dust absorption dominated. $\text{H}\alpha$ has the narrowest lines and thus the highest continuum absorption opacity is not in the blue. We can thus determine a limit on the dust-to-gas ratio in the cocoon: $M_{\text{dust}} \ll \kappa_{\text{bf}}/\kappa_{\text{dust}} M_{\text{gas}} = 10^{-7} M_{\text{gas}}$ (see App. B.6). This is nearly five orders of magnitude less than the dust-to-gas ratio in the Milky Way, and even at metallicities of a few percent solar, as inferred for some of these galaxies, implies significant dust destruction in the ionized gas cocoon (64).

5 Discussion

Using our quantitative framework for modelling LRD-like AGN, we can determine the cocoon’s mass, electron temperature, column density, dust content, continuum absorption opacity, and kinematics. The model also enables the SMBH mass to be estimated from the width of the unscattered broad-line component and the emission radius of the broad lines for a given source luminosity without recourse to low- z scaling relations. This also allows us to measure the Eddington luminosity ratio.

Accounting for electron-scattering broadening, we find the intrinsic width of the broad lines in our sample. Standard AGN scaling relations (65) imply SMBH masses $\log_{10}(M/M_{\odot}) = 5.0\text{--}7.0$. By contrast, Sirocco does not rely on a luminosity–size scaling: the recombination luminosity and measured column density set the cocoon scale, while the unscattered broad-line width gives the Keplerian velocity at that scale. Matching the unscattered components in the sample to our models yields $\log_{10}(M/M_{\odot}) = 5.7 \pm 0.8$ (median with 1σ percentiles). For our sample luminosities, this implies Eddington ratios of $\log_{10}(L/L_{\text{edd}}) = -0.2^{+1.2}_{-0.9}$, implying that most of our sample is accreting close to the Eddington limit. The mass of gas in the ionized cocoon is small: $1\text{--}100 M_{\odot}$ (see Sect. B.3). Typical electron temperatures vary across the cocoon from about 4000 K to about 10 000 K. The hydrogen column densities range from about 10^{24} cm^{-2} to a few 10^{25} cm^{-2} . As mentioned above the dust content in the ionized cocoon is extremely low, essentially negligible. Velocities are $\lesssim 100 \text{ km s}^{-1}$ in the inflow, up to 400 km s^{-1} in the outflow and these two components contain comparable mass-flows.

With such small ionized cocoon masses and high Eddington ratios, the depletion timescale is short, of order a few thousand years, depending on the accretion efficiency. The time for the observed outflows to traverse the cocoon is comparable to this. That is, the wind can clear the cocoon on about the same timescale that the luminous accretion would consume/deplete

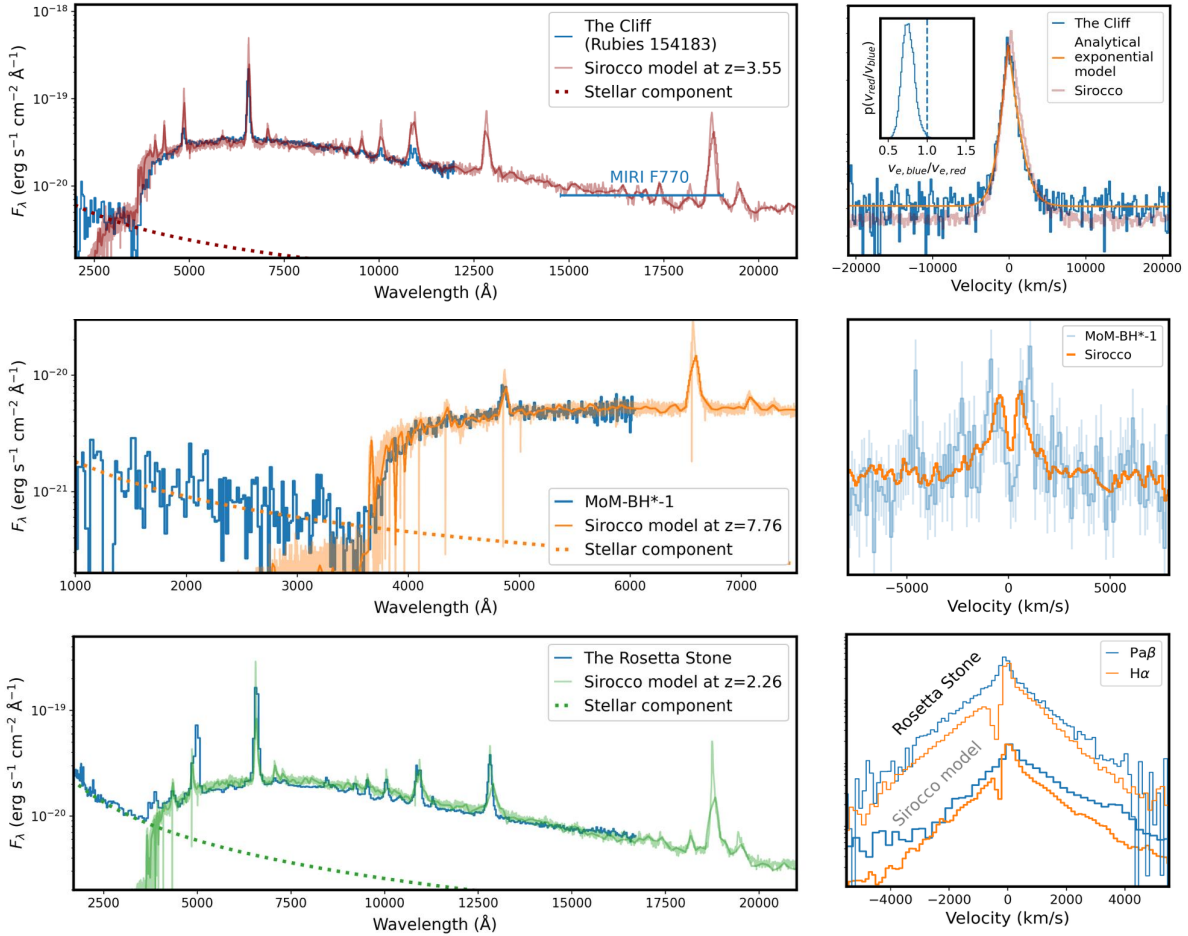


Figure 6: Comparison of the spectra of three extreme LRDs and dust-reddened Sirocco-model spectra, matched for bolometric luminosity and spectral energy distribution (SED) shape. *Left:* the NIRSpec/PRISM spectra (and MIRI F770W photometry) of the noteworthy LRDs, the Cliff (upper; ref (6)), MoM-BH*-1 (middle; ref (14)), and the Rosetta Stone (lower; ref (48)). The Sirocco-model spectra are overplotted and match the SEDs well. *Right:* The $\text{H}\alpha$ lines (and $\text{Pa}\beta$ for the Rosetta Stone) for the NIRSpec grating observations of these sources. The comparison model lines are from the same Sirocco spectra as shown at left for each object. The Sirocco models reproduce the detailed line morphologies, including the exponential wings: for the Cliff, the model reproduces the mild asymmetry, for MoM-BH*-1 the Sirocco model reproduces strong zero-velocity absorption, and for the Rosetta Stone the Sirocco model reproduces broad exponential lines with narrower widths in $\text{H}\alpha$ than $\text{Pa}\beta$ as discussed in ref (60).

its available mass. A much larger gas reservoir is therefore needed to feed the cocoon if the LRD phenomenon is to survive longer than a few millenia. A straightforward extrapolation of the cocoon structure to giant molecular cloud scales ($\sim 30\text{--}100$ pc radius), assuming that the inferred density profile ($\rho \propto r^{-2}$) continues, would yield a total reservoir gas mass $\sim 10^6 M_\odot$. Such a reservoir could withstand the kinetic feedback of the outflow up to perhaps a million years depending on the feedback coupling efficiency. Such a cold, extended gas reservoir would leave high neutral hydrogen column density ($\sim 10^{23}\text{cm}^{-2}$) features imprinted on the cocoon spectrum: Ly α absorption, which might be difficult to detect directly, low-ionisation metal lines such as Na I D and Ca II K, and dust extinction. These latter features may be strong, though much weaker than at solar metallicity, since metallicities are quite low (14, 41, 66, 67). This raises the issue what LRD-like systems would look like at high metallicity. Could low-redshift, high-metallicity LRD-like systems be heavily dust-enshrouded AGN such as Compact Obscured Nuclei (CONs) (68), which could potentially have two or even three orders of magnitude greater dust-to-gas ratios? The exploration of such a connection is outside the scope of this paper, however.

In this model, short-term AGN variability is suppressed smoothing intrinsic variations over the photon diffusion time through the cocoon. This implies variability timescales of

$$t_{\text{var}} \gtrsim 1 \text{ yr} (\tau_{e^-}/10)(R/10^{17}\text{cm}),$$

consistent with the reverberation-tracked photon delays in the Sirocco models. Multi-epoch JWST studies find LRDs are photometrically steady as a population (34, 69), although individual lensed systems do vary: A2744-QSO1 shows broad-line equivalent-width changes at the $\sim 20\%$ level over 2.4 yr rest-frame (70), and R2211-RX1 shows intrinsic colour and brightness variations on 10–100 yr timescales (71). A prediction of our model is that variability should appear on longer timescales only, and most strongly in the *unscattered* cores of the broad lines.

While we have explained in this paper the central properties of LRDs and LRD-like objects quantitatively, many more properties can be elucidated using more detailed modelling. For example, our framework can be used to study the exact nature of the X-ray and radio emission (which are likely to be suppressed by the large gas column), the nature of LRDs at low redshifts, cold gas absorption and dust extinction, and the emission from hot/warm dust near the dust sublimation zone. These properties as well as broader population studies we leave to future work.

References and Notes

1. Y. Harikane, *et al.*, *ApJ* **959**, 39 (2023).
2. M. Killi, *et al.*, *A&A* **691**, A52 (2024).
3. J. E. Greene, *et al.*, *ApJ* **964**, 39 (2024).

4. J. Matthee, *et al.*, *ApJ* **963**, 129 (2024).
5. V. Kokorev, *et al.*, *ApJ* **968**, 38 (2024).
6. A. de Graaff, *et al.*, *arXiv e-prints* p. arXiv:2503.16600 (2025).
7. H. Yanagisawa, *et al.*, *arXiv e-prints* p. arXiv:2601.06015 (2026).
8. D. J. Setton, *et al.*, *arXiv e-prints* p. arXiv:2411.03424 (2024).
9. H. B. Akins, *et al.*, *arXiv e-prints* p. arXiv:2406.10341 (2024).
10. I. Juodžbalis, *et al.*, *arXiv e-prints* p. arXiv:2504.03551 (2025).
11. V. Rusakov, *et al.*, *Nature (in prep)* p. arXiv:2503.16595 (2025).
12. S.-J. Chang, M. Gronke, J. Matthee, C. Mason, *arXiv e-prints* p. arXiv:2508.08768 (2025).
13. K. Inayoshi, R. Maiolino, *ApJ* **980**, L27 (2025).
14. R. P. Naidu, *et al.*, *arXiv e-prints* p. arXiv:2503.16596 (2025).
15. A. de Graaff, *et al.*, *A&A* **684**, A87 (2024).
16. P. G. Pérez-González, *et al.*, *ApJ* **968**, 4 (2024).
17. M. C. Begelman, J. Dexter, *arXiv e-prints* p. arXiv:2507.09085 (2025).
18. Z. Li, K. Inayoshi, K. Chen, K. Ichikawa, L. C. Ho, *ApJ* **980**, 36 (2025).
19. J. Hassan, *et al.*, *arXiv e-prints* p. arXiv:2510.18301 (2025).
20. J. Bellovary, *arXiv e-prints* p. arXiv:2501.03309 (2025).
21. C. Zhang, *et al.*, *arXiv e-prints* p. arXiv:2505.12719 (2025).
22. S. Fujimoto, *et al.*, *Nature* **604**, 261 (2022).
23. R. Maiolino, *et al.*, *A&A* **691**, A145 (2024).
24. V. Kokorev, *et al.*, *arXiv e-prints* p. arXiv:2511.07515 (2025).
25. M. Yue, *et al.*, *ApJ* **974**, L26 (2024).
26. T. T. Ananna, Á. Bogdán, O. E. Kovács, P. Natarajan, R. C. Hickox, *ApJ* **969**, L18 (2024).
27. R. Maiolino, *et al.*, *MNRAS* (2025).
28. G. Mazzolari, *et al.*, *arXiv e-prints* p. arXiv:2412.04224 (2024).

29. A. J. Gloudemans, *et al.*, *ApJ* **986**, 130 (2025).
30. M. Xiao, *et al.*, *A&A* **700**, A231 (2025).
31. P. G. Pérez-González, *et al.*, *ApJ* **968**, 4 (2024).
32. R. Maiolino, *et al.*, *Nature* **627**, 59 (2024).
33. M. Kokubo, Y. Harikane, *arXiv e-prints* p. arXiv:2407.04777 (2024).
34. Z. Zhang, L. Jiang, W. Liu, L. C. Ho, *arXiv e-prints* p. arXiv:2411.02729 (2024).
35. X. Ji, *et al.*, *arXiv e-prints* p. arXiv:2501.13082 (2025).
36. M. Golubchik, *et al.*, *arXiv e-prints* p. arXiv:2512.02117 (2025).
37. A. E. Reines, M. Volonteri, *ApJ* **813**, 82 (2015).
38. F. Pacucci, B. Nguyen, S. Carniani, R. Maiolino, X. Fan, *ApJ* **957**, L3 (2023).
39. E. Durodola, F. Pacucci, R. C. Hickox, *ApJ* **985**, 169 (2025).
40. M. A. Marshall, *et al.*, *A&A* **702**, A50 (2025).
41. A. J. Taylor, *et al.*, *ApJ* **989**, L7 (2025).
42. A. de Graaff, *et al.*, *arXiv e-prints* p. arXiv:2511.21820 (2025).
43. A. Torralba, *et al.*, *arXiv e-prints* p. arXiv:2510.00103 (2025).
44. J. E. Greene, L. C. Ho, *ApJ* **630**, 122 (2005).
45. I. Juodžbalis, *et al.*, *Nature* **636**, 594 (2024).
46. G. P. Nikopoulos, *et al.*, *arXiv e-prints* p. arXiv:2510.06362 (2025).
47. F. D'Eugenio, *et al.*, *arXiv e-prints* p. arXiv:2510.00101 (2025).
48. I. Juodžbalis, *et al.*, *MNRAS* **535**, 853 (2024).
49. A. de Graaff, *et al.*, *A&A* **697**, A189 (2025).
50. K. E. Heintz, *et al.*, *A&A* **693**, A60 (2025).
51. C. Binggeli, *et al.*, *MNRAS* **489**, 3827 (2019).
52. P. Rinaldi, *et al.*, *arXiv e-prints* p. arXiv:2507.17738 (2025).
53. K. S. Long, C. Knigge, *ApJ* **579**, 725 (2002).

54. J. H. Matthews, *et al.*, *MNRAS* **536**, 879 (2025).

55. F. Pacucci, A. Ferrara, D. D. Kocevski, *arXiv e-prints* p. arXiv:2601.14368 (2026).

56. G. J. Ferland, *et al.*, *Rev. Mexicana Astron. Astrofis.* **53**, 385 (2017).

57. E. J. Parkinson, *et al.*, *MNRAS* **540**, 3069 (2025).

58. A. Laor, *ApJ* **643**, 112 (2006).

59. K. Inayoshi, R. Maiolino, *ApJ* **980**, L27 (2025).

60. M. Brazzini, *et al.*, *arXiv e-prints* p. arXiv:2507.08929 (2025).

61. X. Lin, *et al.*, *arXiv e-prints* p. arXiv:2507.10659 (2025).

62. D. Nandal, A. Loeb, *arXiv e-prints* p. arXiv:2507.12618 (2025).

63. D. Kido, K. Ioka, K. Hotokezaka, K. Inayoshi, C. M. Irwin, *arXiv e-prints* p. arXiv:2505.06965 (2025).

64. D. B. Fisher, *et al.*, *Nature* **505**, 186 (2014).

65. A. E. Reines, J. E. Greene, M. Geha, *ApJ* **775**, 116 (2013).

66. R. Maiolino, *et al.*, *arXiv e-prints* p. arXiv:2505.22567 (2025).

67. R. Tripodi, *et al.*, *arXiv e-prints* p. arXiv:2412.04983 (2024).

68. S. Aalto, *et al.*, *A&A* **584**, A42 (2015).

69. W. L. Tee, X. Fan, F. Wang, J. Yang, *arXiv e-prints* p. arXiv:2412.05242 (2024).

70. L. J. Furtak, *et al.*, *A&A* **698**, A227 (2025).

71. Z. Zhang, *et al.*, *arXiv e-prints* p. arXiv:2512.05180 (2025).

72. P. Jakobsen, *et al.*, *A&A* **661**, A80 (2022).

73. D. J. Eisenstein, *et al.*, *arXiv e-prints* p. arXiv:2306.02465 (2023).

74. A. J. Bunker, *et al.*, *A&A* **690**, A288 (2024).

75. F. D'Eugenio, *et al.*, *ApJS* **277**, 4 (2025).

76. P. Arrabal Haro, *et al.*, Environmental effects on galaxy evolution in a z=5.2 proto-cluster, JWST Proposal. Cycle 1, ID. #2674 (2021).

77. D. J. Eisenstein, *et al.*, *arXiv e-prints* p. arXiv:2310.12340 (2023).

78. E. Nelson, *et al.*, Extremely massive galaxies in the early universe: a challenge to Lambda-CDM?, JWST Proposal. Cycle 2, ID. #4106 (2023).
79. K. Glazebrook, *et al.*, How Many Quiescent Galaxies are There at 3, JWST Proposal. Cycle 1, ID. #2565 (2021).
80. P. Arrabal Haro, *et al.*, Spectroscopic follow-up of ultra-high-z candidates in CEERS: Characterizing true $z > 12$ galaxies and $z > 4$ -7 interlopers in preparation for JWST Cycle 2, JWST Proposal. Cycle 1, ID. #2750 (2022).
81. E. Egami, *et al.*, JWST NIRSpec/NIRCam Follow-Up of the High-Redshift Transients Discovered in the GOODS-S JADES-Deep Field, JWST Proposal. Cycle 2, ID. #6541 (2023).
82. H. Atek, *et al.*, *arXiv e-prints* p. arXiv:2511.07542 (2025).
83. K. Ito, *et al.*, *arXiv e-prints* p. arXiv:2506.22642 (2025).
84. C. L. Pollock, *et al.*, *arXiv e-prints* p. arXiv:2506.15779 (2025).
85. R. E. Kass, A. E. Raftery, *Journal of the American Statistical Association* **90**, 773 (1995).
86. J. S. Speagle, *MNRAS* **493**, 3132 (2020).
87. S. Koposov, *et al.*, joshspeagle/dynesty: v2.1.4 (2024).
88. Planck Collaboration, *et al.*, *A&A* **641**, A6 (2020).
89. J. H. Matthews, C. Knigge, K. S. Long, S. A. Sim, N. Higginbottom, *MNRAS* **450**, 3331 (2015).
90. L. B. Lucy, *A&A* **384**, 725 (2002).
91. L. B. Lucy, *A&A* **403**, 261 (2003).
92. S. A. Sim, *MNRAS* **356**, 531 (2005).
93. Z. Yan, K. Inayoshi, K. Chen, J. Guo, *arXiv e-prints* p. arXiv:2512.11050 (2025).
94. R. S. Sutherland, M. A. Dopita, *ApJS* **88**, 253 (1993).
95. G. Barro, *et al.*, *arXiv e-prints* p. arXiv:2512.15853 (2025).
96. K. D. Gordon, G. C. Clayton, K. A. Misselt, A. U. Landolt, M. J. Wolff, *ApJ* **594**, 279 (2003).
97. C. Huang, R. A. Chevalier, *MNRAS* **475**, 1261 (2018).

98. V. V. Sobolev, *Soviet Ast.* **1**, 678 (1957).

99. V. V. Sobolev, *Moving Envelopes of Stars* (1960).

100. U. M. Noebauer, S. A. Sim, *Living Reviews in Computational Astrophysics* **5**, 1 (2019).

101. J. C. Weingartner, B. T. Draine, *ApJ* **548**, 296 (2001).

102. A. J. Cameron, *et al.*, *MNRAS* **534**, 523 (2024).

103. H. Katz, *et al.*, *The Open Journal of Astrophysics* **8**, 104 (2025).

104. G. Münch, *ApJ* **108**, 116 (1948).

105. M. Sekeráš, A. Skopal, *MNRAS* **427**, 979 (2012).

106. D. J. Hillier, *A&A* **247**, 455 (1991).

107. N. Roth, D. Kasen, *ApJ* **855**, 54 (2018).

108. E. J. Parkinson, *et al.*, *MNRAS* **510**, 5426 (2022).

109. Z. Peng, *et al.*, *arXiv e-prints* p. arXiv:2508.03912 (2025).

110. P. W. A. Roming, *et al.*, *ApJ* **751**, 92 (2012).

111. R. M. Humphreys, *et al.*, *ApJ* **760**, 93 (2012).

112. N. N. Chugai, *MNRAS* **326**, 1448 (2001).

113. C. Fransson, *et al.*, *ApJ* **797**, 118 (2014).

114. F. Yuan, R. Narayan, *ARA&A* **52**, 529 (2014).

115. J. K. Jørgensen, *et al.*, *Nature* **606**, 272 (2022).

116. J. E. Greene, *et al.*, *arXiv e-prints* p. arXiv:2509.05434 (2025).

Acknowledgements

We would like to thank Kenta Hotokezaka, Alex J. Cameron and Sune Toft for inspiring discussions. Data, code, and materials availability: The Sirocco code (54) and documentation are provided¹. The comparison to observed LRD makes use of the public *JWST* data collected as part of several observational programs with the NIRSpec spectrograph (72) with the following PIDs; 1181, 1210, 2674, 3215, JADES ref. (73–76); 3215, 4106, 4233, JADES Origins Field ref. (77, 78); 4233, 2565, RUBIES ref. (49, 79–81); 3293, Glimpse ref. (82); 3567, DEEP-DIVE ref. (83); 4318; 5224, MoM ref. (14). These observations have been uniformly reduced

¹<https://github.com/sirocco-rt/sirocco>

and published as part of the Dawn *JWST* Archive² (DJA), (49, 50, 84) or in the case of MoM-BH*-1, kindly provided by R. Naidu et al³. DJA is an initiative of the Cosmic Dawn Center (DAWN), which is funded by the Danish National Research Foundation under grant DNRF140. This work is based in part on observations made with the NASA/ESA/CSA James Webb Space Telescope. The data were obtained from the Mikulski Archive for Space Telescopes (MAST) at the Space Telescope Science Institute, which is operated by the Association of Universities for Research in Astronomy, Inc., under NASA contract NAS 5-03127 for JWST. Funding: AS, DW, RD, KEH and SAS acknowledge funding by the European Union (ERC, HEAVYMETAL, 101071865). Views and opinions expressed are, however, those of the authors only and do not necessarily reflect those of the European Union or the European Research Council. Neither the European Union nor the granting authority can be held responsible for them. RDN is co-funded by Villum Foundation. JHM acknowledges funding from a Royal Society University Research Fellowship (URFR1221062). KEH acknowledges support from the Independent Research Fund Denmark (DFF) under grant 5251-00009B. CK and SAS were supported by the UK’s Science and Technology Facilities Council (STFC, respectively grant ST/V001000/1 and ST/X00094X/1). Author Contributions: AS wrote the manuscript and produced the figures in consultation with DW. AS and JHM developed the Sirocco models in the LRD context with input on radiative transfer from SAS, CK and KL from an original idea by SAS and DW. GN, AS and RD analysed the spectroscopic data and tested the models; NA fit the imaging. GB and KEH reduced the spectroscopic and photometric data. JHM, KEH, SAS and JW helped to improve the manuscript on the radiative transfer modelling, interpretation of the observables and the wider context of supermassive black hole and galaxy evolution. All authors reviewed and edited the manuscript. Competing interests: The authors declare no competing interests.

²<https://dawn-cph.github.io/dja>

³<https://zenodo.org/records/15059215>

A Details of the observed sample

To be included in the LRD sample requires $\Delta\text{BIC} > 10$ for the addition of a broad component. Objects have increasingly strong evidence for electron-scattering broadened lines with increasingly high SNR $\text{H}\alpha$ lines, as quantified by the ΔBIC (Fig. A2). We tested exponential and Gaussian line shapes for these objects following ref (11) and assuming a significance threshold of $\Delta\text{BIC} > 6$ (85). The broad line models compared were: the sum of two Gaussian broad lines (gaus), a double exponential broad line plus a Gaussian unscattered core (exp), or an asymmetric exponential broad line plus a Gaussian electron-scattering outflow (exp_{asym}) with and without absorption components. In each case we also included an additional narrow Gaussian component for $\text{H}\alpha$ and narrow components associated with the [N II] doublet. Thirteen objects clearly favour exponential wing shapes, with seventeen objects statistically indistinguishable, and no object favouring a two-Gaussian parameterization. All objects in the sample with prominent absorption features favour exponential wings significantly. The significance of these best-fitting models is assessed from the χ^2 of the optimized model, computed with DYNESTY (86, 87). The full comparison observational sample is summarized in Fig. A1, which shows JWST/NIRCam imaging and in Table 1, which lists the coordinates, MSAID and spectroscopic setup. Imaging Sersic fits are consistent with predominantly unresolved morphologies. ID 9 and 29 may have a small resolved component (or a close neighbour), but our results are unchanged if they are excluded. Table 1 further reports the best-fitting line-profile models (with the sole exception of rubies-uds1_4233_40579, where only the extreme wings of $\text{H}\alpha$ are covered in the grating making any model distinction insignificant). When converting flux to luminosities we assume the flat ΛCDM -dominated concordance cosmological model (88).

We show an example fit and residual of the two highest SNR $\text{H}\alpha$ lines, Glimpse 17775 and GDN 2674-14, in Fig. A3. We note that these are examples of the predicted asymmetric exponential system, where significant improvements to the χ^2 in the wings of the broad line follows from permitting a steeper profile on the blue side. (24) previously noted asymmetry in the Glimpse 17775 $\text{H}\alpha$ line as likely caused by blueshifted Balmer absorption, but we emphasise that even allowing for absorption in the symmetric wings provides a worse fit, as the asymmetry is a phenomenon extending to the extreme velocity-wings of the line at ± 3000 km/s. It is worth emphasising that this asymmetry is significant despite freedom in fitting the broad-line center offset from the host or narrow-line redshift. For most objects the large degeneracy in asymmetry and the broad-line centroid center inflates the errorbars and permits the individual objects to be consistent with symmetry within 2σ (see Fig. 1 right panel, although we note all these LRDs show steeper blueward slopes if we do not permit the centroid to drift redward by $\gtrsim 100$ km s $^{-1}$).

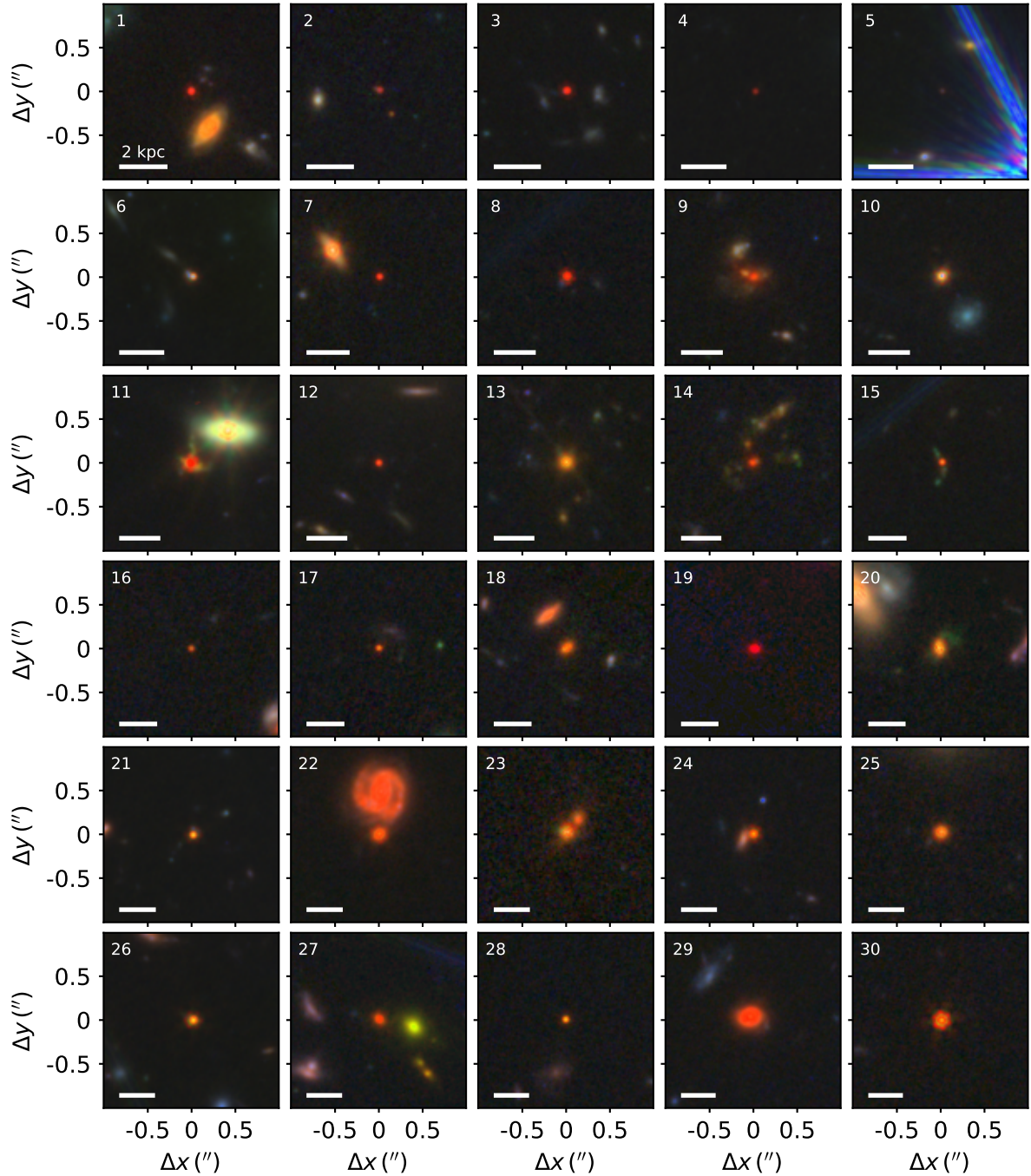


Fig. A1: *JWST/NIRCam* images of the observed sample. While objects were only selected on Balmer break strength and broad H α emission lines, almost all objects are compact and red, with occasional extended blue emission.

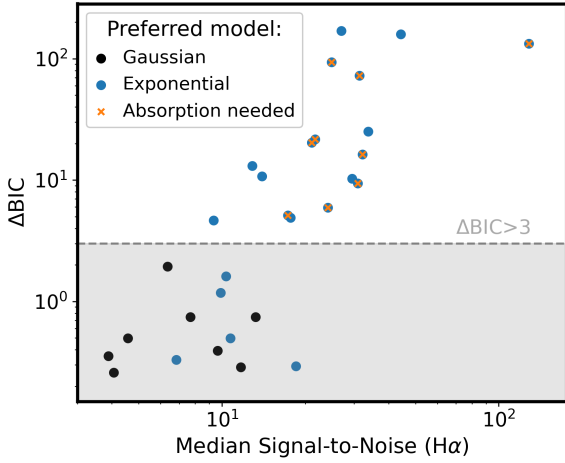


Fig. A2: The ΔBIC between $\text{H}\alpha$ broad line fits with two Gaussians (e.g. Doppler-motion dominated) compared to a single Gaussian convolved with an exponential (electron-scattering dominated). Orange cross indicates objects with evidence for absorption features.

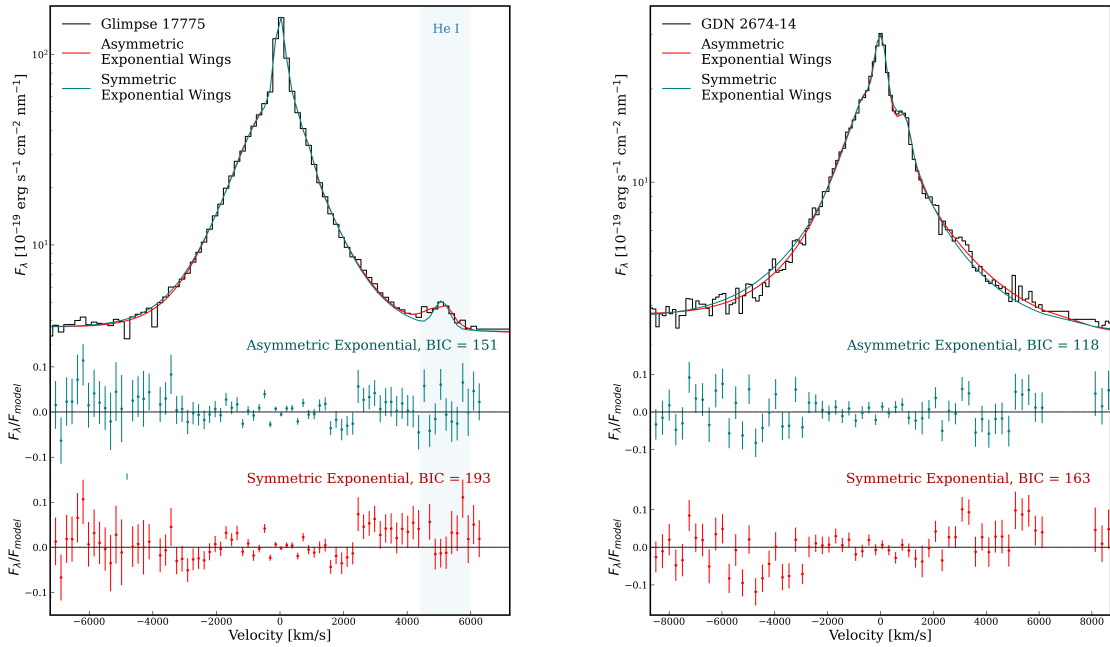


Fig. A3: Example fit and residual structure of (a)symmetric electron-scattering wings for the two highest SNR $\text{H}\alpha$ lines Glimpse 17775 (24) and GDN 14. While the symmetric electron-scattering model is superior to the double Gaussian broad line ($\Delta\text{BIC} > 100$), the asymmetric electron-scattering wings is further superior to the the symmetric model ($\Delta\text{BIC} = 42$ and $\Delta\text{BIC} = 45$). The direction of asymmetry is as predicted for a net outflow.

Table 1: NIRSpec target sample giving redshifts, coordinates, and the best-fit model for H α . The ΔBIC for different model fits with respect to the best-fit model are given. Rubies 4233-40579 is equally well-fit by all models as it is near the edge of the grating.

ID	z	MSAID	α (°)	δ (°)	best-fit	ΔBIC					
			model	exp	exp _{abs}	gaus	gaus _{abs}	exp _{asym}	exp _{asym,abs}		
1	6.9831	rubies-egs61_4233_55604	214.9830256	52.9560013	exp _{abs}	781.9	—	645.2	21.7	1048.7	2.7
2	6.7596	jades-gdn2_1181_954	189.1519657	62.2596352	exp	—	12.2	4.7	16.3	9.1	16.6
3	6.6849	rubies-egs63_4233_49140	214.8922479	52.8774097	exp _{abs}	233.2	—	243.4	5.9	239.2	6.1
4	6.2230	glimpse-obs01b_9223_5536	342.2562866	-44.5601196	exp	—	11.2	0.3	11.6	3.3	14.8
5	6.1080	glimpse-obs01_9223_12248	342.2319946	-44.5489082	gaus	0.4	15.4	—	16.1	5.2	21.5
6	6.1050	glimpse-obs02_9223_41948	342.1908569	-44.5374870	exp _{abs}	165.8	—	378.5	16.3	170.4	0.6
7	5.5819	rubies-uds23_4233_172350	34.3689512	-5.1039415	exp _{abs}	46.9	—	74.7	10.7	23.1	5.6
8	5.2771	rubies-egs53_4233_42046	214.7953678	52.7888466	exp _{asym,abs}	975.6	2.1	839.7	72.4	958.4	—
9	5.2215	rubies-uds23_4233_148866	34.3264335	-5.1373819	gaus	1.9	12.2	—	13.2	5.8	17.3
10	5.1833	gdn-pah123_2674_14	189.1998118	62.1614741	exp _{asym}	13.1	12.9	159.5	165.0	—	2.9
11	5.0389	jades-gdn_1181_68797*	189.2291371	62.1461898	exp _{abs}	997.0	—	946.0	93.4	971.2	2.2
12	4.9520	valentino-egs_3567_42232	214.8867922	52.8553805	exp _{abs}	44.7	—	43.2	1.2	42.9	1.8
13	4.8977	rubies-egs61_4233_75646	214.9155459	52.9490183	exp _{asym,abs}	35.7	12.9	35.9	13.1	40.9	—
14	4.8075	rubies-uds43_4233_19735	34.3010942	-5.2879853	gaus	0.3	5.0	—	7.7	5.7	7.4
15	4.2239	rubies-egs63_4233_28812	214.9241491	52.8490503	exp _{abs}	96.9	—	39.6	5.1	56.3	5.4
16	4.1478	rubies-uds22_4233_119957	34.2689076	-5.1767218	exp	—	11.7	1.6	14.8	5.3	20.5
17	4.1293	rubies-uds1_4233_31747	34.22237573	-5.2602446	exp _{abs}	2.1	—	1.2	0.5	5.0	4.5
18	4.0949	rubies-uds23_4233_155916	34.3170308	-5.1276114	gaus	0.3	14.4	—	14.2	5.1	16.0
19	3.9853	valentino-obs08_3567_18	34.3161903	-5.0514412	exp _{asym,abs}	69.6	11.4	68.2	20.4	67.8	—
20	3.9428	gto-wide-uds13_1215_3757*	34.3225421	-5.1713913	gaus	0.5	13.2	—	11.9	6.8	17.8
21	3.7473	glimpse-obs01b_9223_43084	342.2333984	-44.5390587	exp _{asym}	3.4	16.8	30.2	25.1	—	14.4
22	3.6486	rubies-egs62_4233_58237	214.8505715	52.8660296	exp	—	3.1	0.3	2.0	5.0	7.9
23	3.5936	cosmos-alpha_4318_126891	150.4862003	2.4279533	exp _{asym,abs}	138.6	2.2	18.1	9.4	143.3	—
24	3.5454	rubies-uds31_4233_154183	34.4107486	-5.1296643	exp _{asym,abs}	9.8	1.5	12.8	10.3	11.8	—
25	3.5421	gto-wide-uds14_1215_5238*	34.2937549	-5.2269936	gaus _{abs}	19.5	0.7	18.5	—	25.6	6.9
26	3.5026	glimpse-obs02_9223_17775	342.2008057	-44.5436592	exp _{asym,abs}	705.2	203.5	723.7	133.0	482.0	—
27	3.4531	rubies-egs53_4233_42482	214.8377242	52.8200405	gaus	0.4	14.6	—	17.2	5.4	20.9
28	3.3538	rubies-uds23_4233_144195	34.3251559	-5.1436853	gaus	0.7	8.2	—	9.0	5.0	13.7
29	3.1292	jades-gdn2_1181_22456	189.0357220	62.2431536	exp _{asym}	17.2	4.6	17.0	4.9	—	9.9
30	3.1073	rubies-uds1_4233_40579	34.2441997	-5.2458714	—	—	—	—	—	—	—

*These objects were observed with the g395h grating, whereas all the rest were observed with the g395m.

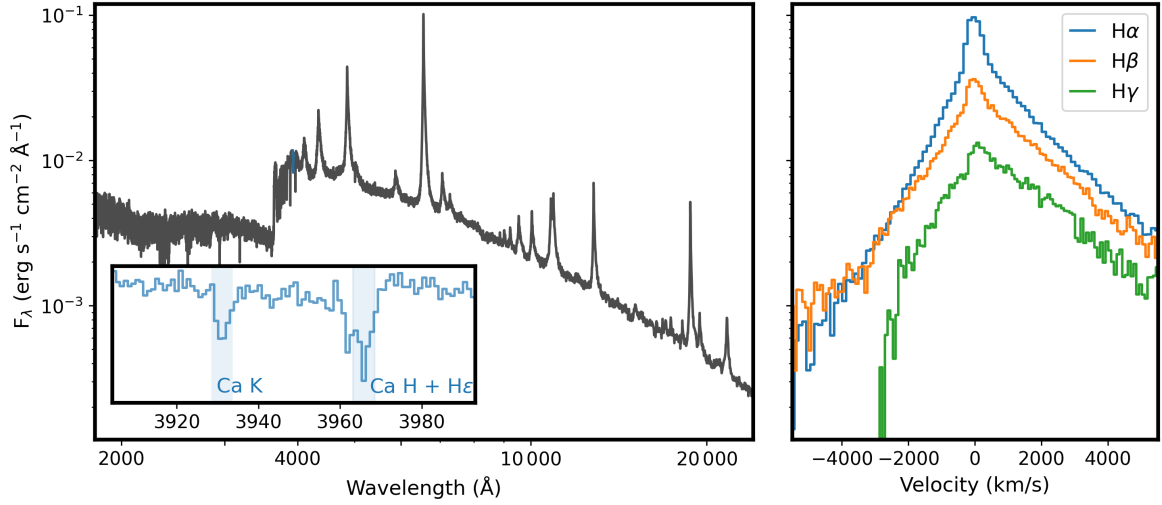


Fig. B1: Example model spectrum of an LRD-like object computed with `SIROCCO`, with prominent hydrogen emission lines and Ca H and K lines highlighted. Even though the model is kinematically spherical (i.e. 1D), it reproduces several characteristic features of observed LRDs, including (i) the Balmer break, (ii) broad hydrogen and helium emission lines with exponential line profiles, and (iii) self-absorption in the permitted lines, with a pronounced P Cygni feature in H α . The parameters for this model are $L = 10^{45}$ erg s $^{-1}$, $\tau_{e^-} \approx 5$, $R_{\text{inner}} = 10^{17}$ cm, and $v_{\text{outflow}} = 100\text{--}500$ km s $^{-1}$ and viewed from a distance of 100 pc. Conditions sufficient to produce a Balmer-break and self-absorption naturally produce electron-scattering-broadened lines. There are two things to note here. First, even though electron scattering, which is largely independent of wavelength, dominates the broadening mechanism, the different hydrogen line profiles are not identical. Second, the lines are strongly asymmetric due to the spherical outflow (see §C).

B Sirocco model structure

B.1 Atomic data and radiative transfer mode

The electron-scattering module in `SIROCCO` has been validated both in previous studies (57) and via direct comparison with the independent electron-scattering code of ref (11). Resonance scattering is included using an escape-probability formalism, but it contributes only a minor fraction of the total scattering in all models considered. We use the ‘hybrid macro-atom’ radiative transfer mode in `SIROCCO` (54, 89). In this mode, we adopt the full macro-atom formalism (89–92) for H and He, which includes all the important bound-free and bound-bound processes, but treat metals as ‘simple atoms’, wherein recombination is less accurately modelled and line transfer is treated with a two-level approximation. We employ a thermal-trapping method for anisotropic scattering and note that the Sobolev approximation treatment only applies to line transfer. As

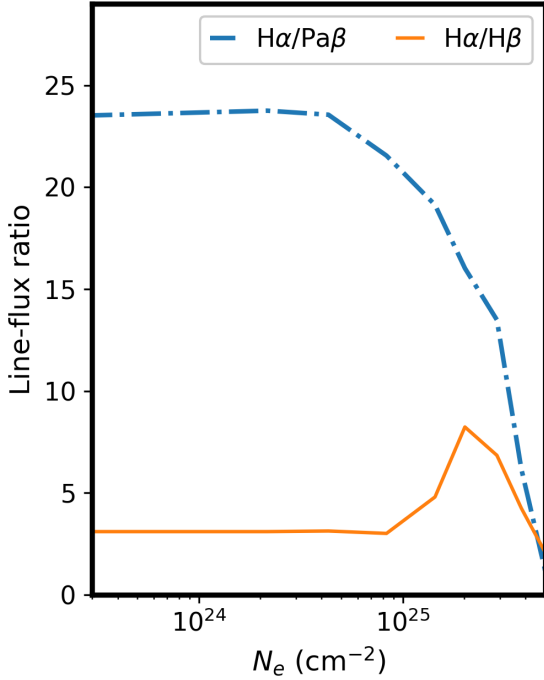


Fig. B2: Line ratios of $H\alpha/Pa\beta$ and $H\alpha/H\beta$ from a sequence of Sirocco spherical models with different column densities in a homologous wind. Electron-scattering wings require a lower column density ($N_e \gtrsim 10^{24} \text{ cm}^{-2}$) compared to the column densities needed to produce Balmer breaks and Balmer line absorption ($N_H \gtrsim 10^{25} \text{ cm}^{-2}$). The high-column-density regime with all three effects are characterised by strong deviations from Case B line ratios.

the interior beneath the cocoon is not thermally solved, photons that reach the inner boundary are reflected. We include the following elements within Sirocco: H, He, C, N, O, Ne, Na, Mg, Al, Si, S, Ar, Ca and Fe. H and He levels are included up to principal quantum numbers $n = 20$ and $n = 10$, respectively (providing high-fidelity for Balmer physics) and two-level approximation for line transfer for metals, with cross-sections/lines/collisions from the bundled datasets. Fig. B1 illustrates the high-equivalent-width absorption features (e.g. Ca II) that can form in a cold cocoon, as observed in “the Egg” LRD (61), and Fig. B2 shows the observed deviations from Case B recombination ratios expected under dense gas conditions (46, 47, 93). At low electron temperatures, the thermal balance is a competition between primarily bound-free heating and line cooling. As Sirocco omits some heating/cooling processes at low temperatures, the resulting temperature structure can differ from a more complete treatment. For a more detailed explanation of parameters, code assumptions and atomic data we refer the reader to ref (54).

B.2 Sirocco parameter-space

The cocoon should produce a column density of electrons, $N_e \sim 10^{24} \text{ cm}^{-2}$, as suggested by the observationally inferred Thomson optical depths, $\tau_{e^-} = \sigma_T N_e$ of order unity (11). Expressed as a spherical mass-loss rate, this corresponds to $\dot{M} \sim 0.01 \left(\frac{1}{f_e}\right) \left(\frac{v}{10^7 \text{ cm/s}}\right) \left(\frac{R_{\text{in}}}{10^{15} \text{ cm}}\right)^2 \frac{M_{\odot}}{\text{yr}}$ (where f_e is the mean degree of ionisation). This cocoon will be responsible both for reprocessing the incident radiation field into recombination-line emission and the broadening of these lines via electron scattering. The full list of parameters explored is summarised in Table 2. We discuss the observable imprints of each parameter below, and then outline the preferred model.

Surrounding gas cocoon: We initialize a spherical cocoon with an inner radius $R_{\text{in}} \in [10^{15},$

10^{17}] cm and an outer radius much larger than this (i.e. $R_{\text{out}} = 10R_{\text{in}}$ with larger distances providing similar results due to the steep density slopes). We explore a broad range of power-law slopes $1 < \alpha < 4$, but for our fiducial setup $\rho \propto r^{-2}$. Although mass-loss rate, velocity, and acceleration-structure are physically interdependent, we vary $\rho(r)$ and $v(r)$ independently to explore the observable consequences of each separately. The gas composition is a variable parameter: for our fiducial setup we adopt solar abundances, but also explore sub-solar metallicities, $Z = 10^{-3} - 1 Z_{\odot}$, since metal-poor gas cools less efficiently (94) and thus yields broader exponential electron-scattering wings at fixed Thomson optical depth due to the higher electron temperatures. See Fig. B3 for the functional impact of these parameters on the line profile.

Cocoon kinematics: We parameterize the cocoon gas outflow with a velocity profile $v_{\text{outflow}}(r)$, adopting either a constant velocity, a β -law wind, or homologous expansion. The observations are relatively insensitive to the velocity parameterization, as the both exponential wings and Balmer line absorption are predominantly dictated by the average velocity. Beyond basic spherically symmetric velocity models, we look at multi-component axisymmetric models with independent velocities, densities, and solid-angles (see App. C). We also include a non-zero rotational component v_{ϕ} , where we assume Keplerian motion around the SMBH, $v_{\phi} = \sqrt{GM_{\text{BH}}/r} \sin(\theta)$, where $\sin(\theta)$ accounts for the component of gravitational acceleration towards the rotational axis. For a sufficiently large SMBH or a nearby cocoon, this means that the dominant broadening of the unscattered component is the Doppler motion (see Fig. B5). We assume black hole masses $M_{\text{BH}} \sim 10^{5-8} M_{\odot}$, consistent with revised estimates of the intrinsic H α broad-line width after accounting for broadening from electron scattering (11).

Input radiation field: The total luminosity ($L \simeq 10^{43}-10^{45} \text{ erg s}^{-1}$), especially blueward of the Lyman limit, impacts the mass of ionized gas and the radius to which the cocoon is ionized and thus what the electron column density is. The accretion emission is assumed to be a blackbody with characteristic temperature $T_{\text{BB}} \sim 10^5 \text{ K}$, isotropically emitted in $d\Omega = 4\pi$. However, the results are robust to order-of-magnitude variations in T_{BB} , as the ionisation balance and radiation field are solved self-consistently within the gas, where the flow typically cools to $O(10^4 \text{ K})$.

Multiple components: As we explore broad ranges of geometries and cocoon structures, we use imported models in Sirocco. This accommodates multi-component set-ups with both inflows and outflows. The imported polar coordinate grids are uniformly sampled in θ and logarithmically in r , while the velocity-field reproduces the standard Sirocco coasting wind or homologous expansion. For the kinematic and geometric discussion in this paper, we are mainly concerned with the characteristic velocities in the scattering cocoon, which makes higher-order effects such as the parameterization of the radial velocity less important. In Fig. B4, we show an example two-component model, where the left panel shows the output electron temperature at various spatial positions and highlights that although here we invoke a steep gradient between inflows and outflows, the resulting temperature solution does not display unphysical structures surrounding the shear layer. The central and right panels indicate the input density and velocity structure of the cocoon.

Dust extinction: While the ionised cocoon providing electron scattering is inconsistent with

Table 2: Parameter ranges explored in the SIROCCO run suite. The parameters of the example model spectrum in Fig. B1, which is a model constructed to highlight the diverse and complementary LRD observables, i) balmer break, ii) heterogenous, exponential hydrogen line-profiles and iii) absorption from metals.

Category	Parameter	Description	Fig. B1	Range explored
Input radiation field	M_{BH}	Black-hole mass	$10^7 M_{\odot}$	$10^5-10^8 M_{\odot}$
	L_{BH}	Accretion luminosity	$10^{44} \text{ erg s}^{-1}$	$10^{43}-10^{45} \text{ erg s}^{-1}$
	T_{BB}	Input blackbody temp.	10^5 K	$7 \times 10^3-10^7 \text{ K}$
Cocoon structure	R_{in}	Inner cocoon radius	10^{16} cm	$10^{15}-10^{18} \text{ cm}$
	R_{out}	Outer cocoon radius	10^{17} cm	$10-100 R_{\text{in}}$
	ρ	Density at R_{in}	$10^{10} \text{ g cm}^{-3}$	$10^6-10^{11} \text{ g cm}^{-3}$
	α	Density power-law	2	1-4
	Z	Metallicity	$1 Z_{\odot}$	$10^{-3}-1 Z_{\odot}$
	v_{out}	Outflow velocity	100 km s^{-1}	$50-1000 \text{ km s}^{-1}$
Multiple components	$\frac{d\Omega_{\text{inflow}}}{d\Omega_{\text{outflow}}}$	Solid-angle ratio	0	0-5
	$\frac{v_{\text{inflow}}}{v_{\text{outflow}}}$	Velocity ratio	–	0-5
	$\frac{\rho_{\text{inflow}}}{\rho_{\text{outflow}}}$	Density ratio	–	0-5

significant dust (see Sect. B.6), the diversity of red spectral slopes, e.g., (95), and the conditions permitting dust at larger radii motivate the additional freedom to add reddening. In this work, we apply modest dust extinction ($0.3 < A_V < 0.7$) with SMC extinction curve (96) in Fig. 6, but otherwise show SIROCCO model outputs without this added degree of freedom.

Preferred models: The luminosity of the reprocessed red optical emission is set by the total ionised mass, which is noteworthy as it allows us to functionally decouple the question of LRD luminosity and spectral shape. In particular, a coherent re-scaling of i) cocoon size, ii) wind mass-loss rate ($\propto \rho/r^2$) and iii) input luminosity provides similar columns and thus spectral shapes, but a correspondingly rescaled output luminosity. Conversely, the Balmer break and scattering wings constrain the column of $n = 2$ and ionised gas respectively. These are naturally connected, which is why picking the closest line-shape SIROCCO models also provided a good match for the overall spectral continuum shape (i.e. as done in Fig. 6). In this work, for comparisons to observed LRDs, we used i) the observed H α line-shapes to find the closest LRD model spectra in terms of kinematics and column of cocoon material and ii) rescaled the cocoon scale to match the observed luminosity. In future work, higher-detail fitting can be employed with a more complete LRD-template basis, which could access the exact spectral shape of the continuum, absorption of metals, etc.

B.3 Gas mass and temperature – width of scattered broad lines

The velocity width of the exponentially broadened lines is set primarily by the electron column density and temperature: these determine respectively the number of scatterings and the veloc-

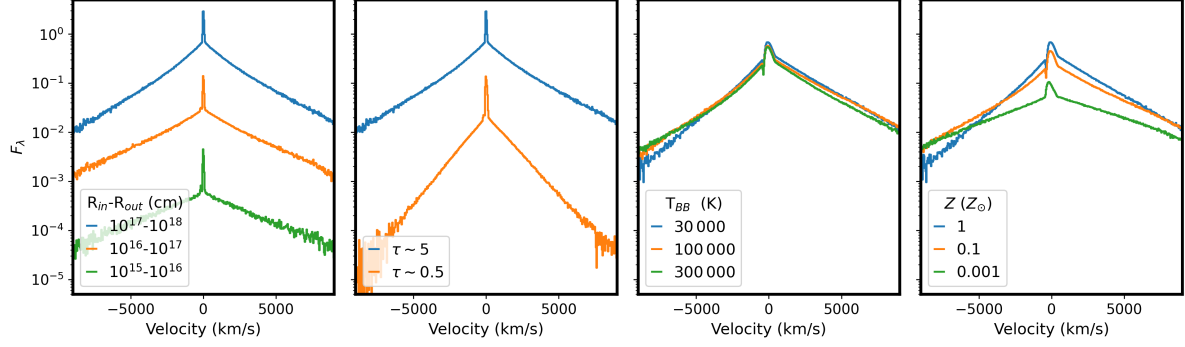


Fig. B3: Example H α lines in Sirocco spherical models varying i) the characteristic radius (for a fixed hydrogen column density), ii) the density (or equivalently the depth optical depth), iii) temperature of the input radiation field and iv) metallicity of the cocoon. The two-left most panels shows order-of-magnitude differences in line luminosities because larger densities imply larger recombination-line fluxes.

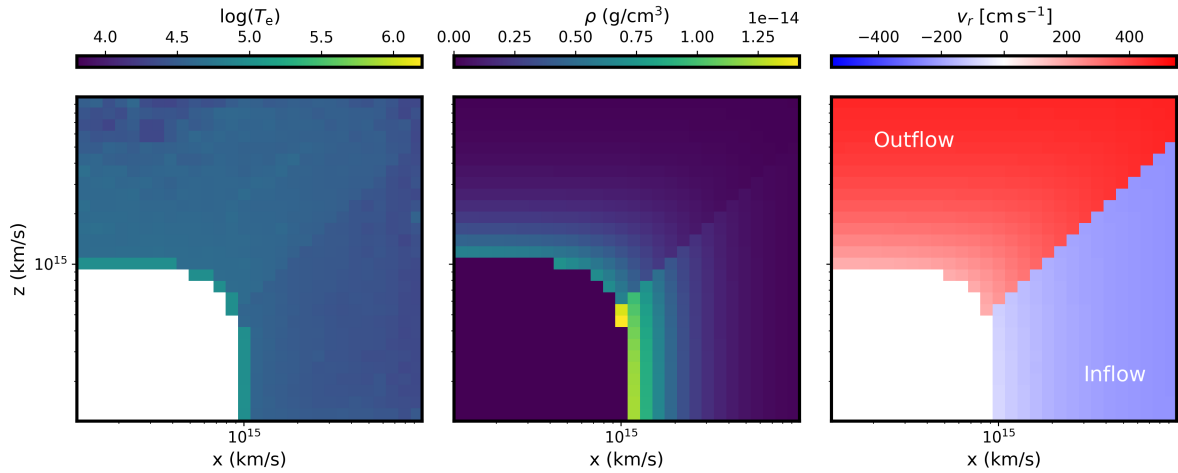


Fig. B4: Electron temperature map in the 2d plane for an inflow/outflow model (left). The model is based on the input density and velocity fields shown (centre and right respectively), where the inflowing equatorial gas is denser and slower than the outflowing polar gas.

ity shift per scatter. Continuum absorption, by contrast, controls the survival rate of photons, especially multiply scattered photons.

Varying the electron column density produces a range of different spectra, see Fig. 3. The column density required for an electron-scattering optical depth of order unity is comparable to or smaller than the hydrogen column densities implied by the Balmer break and Balmer self-absorption (14, 41) even for a modest ionisation fraction $f_e \gtrsim 0.1$. Fig. B3 (first panel) shows the exponentially broadened lines for a cocoon at three spatial scales for fixed $\tau_{e^-} \sim 5$, which illustrates the cocoon’s spatial scale is not tied to spectral shape but to the luminosity. The subtle differences in exponential slopes arise because higher-density models have greater absorption opacity and thus absorb photons in the scattering wings. Varying the cocoon’s volume density (Fig. B3, second panel) changes the optical depth and therefore the width of the exponential wings, see for example Fig. 3 of ref. (97). High column densities can be achieved with relatively little mass. Given, i) $N_e = \int n_e(r) dr$, ii) total number of electrons $N_{e,tot} = \int n_e(r) dV$, and iii) total mass $M_{\text{cocoon}} = \mu m_H f_e N_{tot}$, we obtain:

$$M_{\text{cocoon}} \approx 1 M_\odot \left(\frac{R_{in}}{10^{16} \text{ cm}^{-2}} \right)^2 \left(\frac{f_e}{1} \right) \left(\frac{1-\alpha}{3-\alpha} \right) \quad (1)$$

where the prefactor $\left(\frac{1-\alpha}{3-\alpha} \right)$ comes from integrating $n_e \propto r^{-\alpha}$ assuming $\alpha > 3$. Conversely, for the wind-like structure, $\alpha = 2$, we would get an additional factor of R_{out}/R_{in} . In all cases, however, only a relatively modest cocoon mass is required compared to the SMBH mass to produce the observed characteristic features. This does not mean, however, that the full accreting gas cloud may not be much more massive, and indeed, it must be to continue to feed the accretion onto the SMBH for longer than a few centuries.

The velocity shift per scattering is harder to modify. Efficient cooling keeps the gas near $\lesssim 10^4$ K. For instance, varying the input radiation field from the SMBH under the blackbody ansatz (Fig. B3, third panel) ultimately has only a minor effect on the resulting effective width of the lines. The equilibrium T_e can be affected by gas metallicity, as cooling can become inefficient at $\gtrsim 10^5$ K in very low metallicity systems (Fig. B3, fourth panel). It is possible in principle to constrain the electron-scattering optical depth independent of the line width based on the ratio of unscattered to total line photons. If we trust this measure, we would infer the observed sample to have $\tau_{e^-} \sim 2$. This optical depth requires a relatively low temperature, $T_e \sim 5,000$ K, to match the observed widths. This relatively cool gas is consistent with independent temperature estimates from Fe II, $T_{\text{eff,Fe II}} \sim 7,000$ K (43) and Ca triplet absorption $T_{\text{eff,Ca T}} \sim 5,000$ K (61).

B.4 SMBH mass – Width of the unscattered line

The unscattered component of the broad lines still encodes information about the intrinsic Doppler motion of the gas and thus, by extension, the SMBH mass (Fig. B5). The radial outflow/inflow velocities and potential turbulent velocities can contribute to the width of the unscattered line at the level of a few hundred km/s, but the Keplerian rotation is the only mechanism here which permits velocities on the order of thousands of km/s. The unscattered veloc-

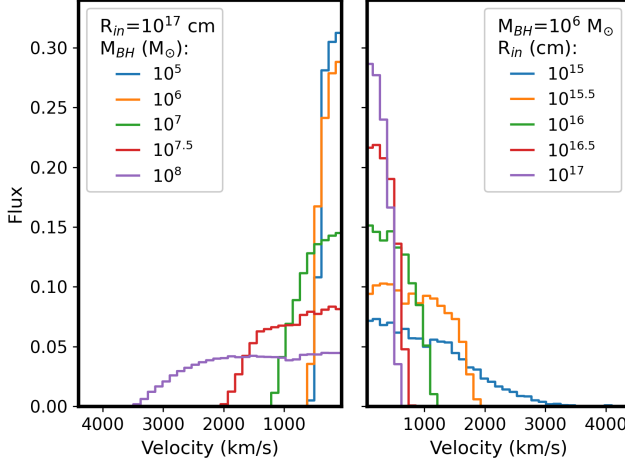


Fig. B5: H α profile without scattering as a function of SMBH mass (left) and gas cocoon proximity (right). The central (unscattered) H α line becomes increasingly broad with increasing SMBH mass. A similar broadening effect is produced by shrinking R_{in} , because the relevant Keplerian velocity, v_{Kep} , is $v_{\text{Kep}} \propto M_{BH}^{1/2} R_{in}^{-1/2}$.

ity can reach thousands of km/s for a sufficiently massive SMBH ($\gtrsim 10^7 M_{\odot}$ at $R \sim 10^{17}$ cm) or more compact cocoons ($\lesssim R \sim 10^{16}$ cm even for $10^6 M_{\odot}$). The observed sample, however, shows unscattered cores of 300_{-200}^{+500} km s $^{-1}$ consistent with low-mass SMBHs ($\sim 10^6 M_{\odot}$).

B.5 Sobolev criterion

An operational assumption within SIROCCO is the Sobolev approximation (98, 99), which applies when the resonance region of the bound-bound interactions (the Sobolev length scale) is small compared to the other relevant scales of the system. In particular, the Sobolev length scale is set by the thermal speed of the ions, $v_{\text{ion,th}}$, relative to the characteristic velocity gradient $|dv/dr|$. For a typical temperature (10⁴ K), a cocoon scale, R , and a homologous velocity scale with $v_{\text{outflow}} = v(R)$, the Sobolev length in spherical symmetry becomes:

$$l_s = \frac{v_{\text{ion,th}}}{|dv/dr|} = 10^{14} \text{ cm} \left(\frac{R}{10^{16} \text{ cm}} \right) \left(\frac{v_{\text{outflow}}}{1000 \text{ km/s}} \right)^{-1} \left(\frac{v_{\text{ion,th}}}{10 \text{ km/s}} \right) \quad (2)$$

using $|dv/dr| \approx v_{\text{outflow}}/R$ for a homologous outflow. In the more general case, including a coasting flow where $dv/dr = 0$, the term that sets how quickly one passes over the resonance region, e.g. $(dl/dv)_{r_s} = c/v_{lu}((1 - \mu^2)v/r + \mu^2 dv/dr)_{r_s}^{-1}$, the velocity gradient is of the same order of magnitude, except for directions very close to radial (100). Importantly, the Sobolev scale remains much less than the characteristic scale of the system, the scale over which the ionisation or the temperature change, and it is smaller than the grid scale when we fiducially parameterize the cocoon structure at 10–50 radial positions. For small characteristic velocities, $\ll 100$ km/s, we leave the microscopic regime for which SIROCCO is designed. However, even in this regime the electron scattering (e.g. discussions of asymmetry, kinematics and geometry) would still be robust.

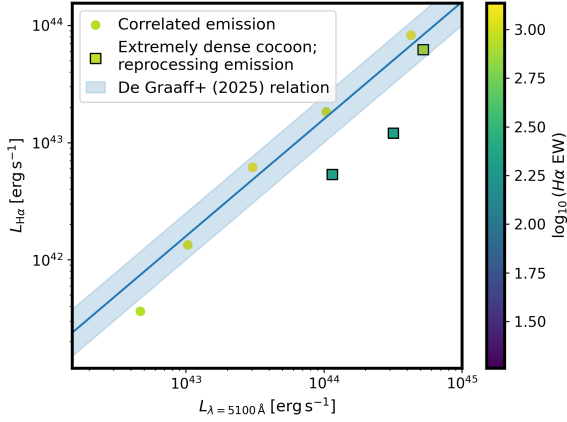


Fig. B6: $H\alpha$ line luminosity as a function of continuum luminosity at 5100\AA . These SIROCCO model outputs are correlated with similar offset and slope as the observational sample in ref (42). The drop-off found by ref (42) is also reproduced for the extremely dense cocoons, when the recombination lines begin to be reprocessed.

B.6 Bound-free opacity in SIROCCO

The SIROCCO models predict variations in broad-line widths between $H\alpha$ and other hydrogen lines. In the main text, we mention that this is because the continuum bound-free absorption opacity varies with wavelength and the lower bound-free-opacity at $H\beta$ compared to $H\alpha$ means less reprocessing and thus broader exponential lines (see Fig. B7). We reached this conclusion as follows. The linewidths may differ due to two effects. i) Line formation at different cocoon depths, so that the lines see different column densities (12), or ii) Continuum absorption is wavelength-dependent, affecting the opacity of the multiply-scattered photons that populate the exponential wings differently for different lines (97). The strong wavelength-dependence of bound-free opacity ($\propto \lambda^3$ above the photoionisation edge) means that lines closest to the relevant photoionisation edges (e.g. $H\alpha$ is closer to the Paschen edge than $H\beta$), suffer the largest continuum absorption losses to their wings. In the SIROCCO-model spectra, these two causes of differences in linewidths can be separated explicitly, and we find that the continuum opacity dominates. The median $H\alpha$ photon escapes farther out than $H\beta$, but similar to or farther in than $Pa\beta$ (Fig. 2, upper right). So while $H\alpha$ photons traverse a similar or larger electron column than $Pa\beta$, the $H\alpha$ line is observed to be narrower than $Pa\beta$ in the sample objects and in the models due to the bound-free continuum opacity.

B.6.1 Dust-to-gas ratio

In the main text, we also note that we can infer a dust-to-gas ratio in the ionized gas cocoon. Since we can see that the sequence of observed widths is not monotonic with wavelength, this tells us that dust absorption does not dominate (i.e. it is not generally true in the observations that $v_{e,H\beta} < v_{e,H\alpha} < v_{e,Pa\beta}$). This implies dust absorption opacity at $H\beta$ is much less than continuum bound-free opacity at $H\alpha$ within the gas responsible for scattering. This permits a

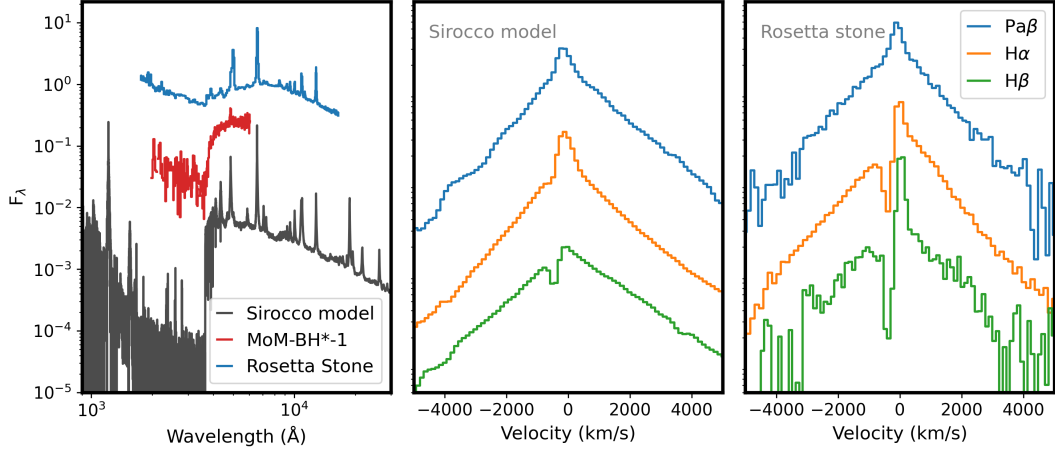


Fig. B7: Example Sirocco spectrum alongside two notable LRDs *Rosetta Stone* (48) and *MoM-BH*-1* (14). The central and right panels show hydrogen line shapes respectively for the Sirocco model spectrum (convolved with the spectral resolution of the *JWST* medium resolution grating) and the *Rosetta Stone* LRD. While electron-scattering cross-section is largely independent of wavelength at these energies, the resulting broadened lines are not identical—in particular $H\alpha$ is narrower than $H\beta$ and $Pa\beta$ —because $H\alpha$ is more sensitive to continuum absorption, reducing the escaping flux of multiply-scattered photons that populate the largest velocities in the wings.

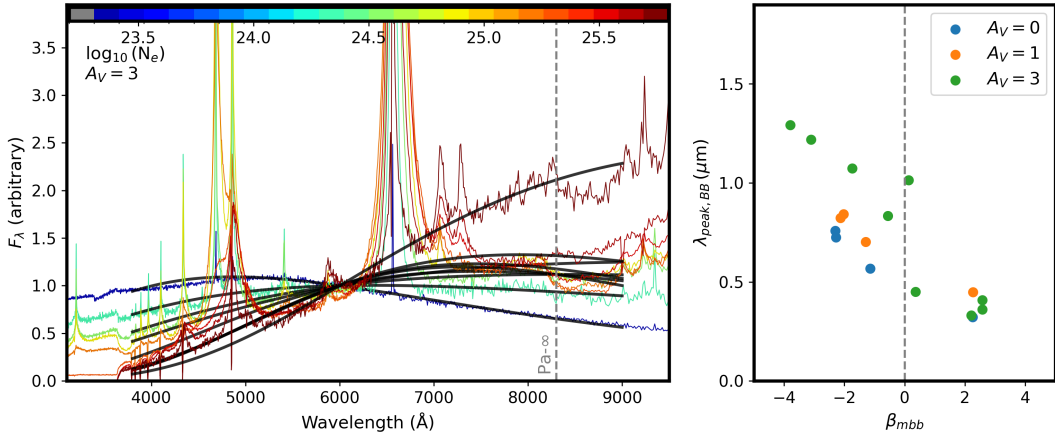


Fig. B8: Blackbody fits to Sirocco models. *Left*: Sequence of Sirocco models with varying column densities fit with modified Planck functions. *Right*: Blackbody peak wavelength as a function of the modification to spectral slope, β_{mbb} . The Sirocco models reproduce a similar range of spectral peak wavelengths and β_{mbb} values and apparent correlations between these as the LRD sample in (42), though the spectra are not blackbodies.

direct observational limit on the dust-to-gas ratio:

$$\frac{M_{dust}}{M_{gas}} \ll \frac{\kappa_{gas,bf}(H\alpha)}{\kappa_{dust}(H\beta)} = \frac{n_3 \sigma_{bf}(H\alpha)}{\rho} \frac{1}{\kappa_{dust}(H\beta)} = \frac{f_{n=3} \sigma_{bf}(H\alpha)}{\mu m_p} \frac{1}{\kappa_{dust}(H\beta)} \quad (3)$$

where ρ is gas density, n_3 is the hydrogen density in $n = 3$, $f_{n=3}$ is the fractional population, m_p is the proton mass and $\sigma_{bf}(H\alpha)$ is the bound-free opacity evaluated at the $H\alpha$ wavelength. The dust-absorption opacity can be estimated from the Milky Way dust-to-gas ratio ($\frac{M_{gas}}{M_{dust}} \approx 100$) and the extinction optical depth per gas mass ($\tau_{H\beta}/(N_H \mu m_p) \approx 100 \text{ cm}^2/\text{g}$), e.g. ref. (101):

$$\kappa_{dust}(H\beta) = \kappa_{gas,dust}(H\beta) \frac{M_{gas}}{M_{dust}} = \frac{\tau_{H\beta}}{\mu m_p N_H} \frac{M_{gas}}{M_{dust}} = 10^4 \text{ cm}^2/\text{g} \quad (4)$$

The implied dust-to-gas mass ratio in LRD cocoons is $\frac{M_{dust}}{M_{gas}} \ll 10^{-7}$ for our SIROCCO $f_{n=3}$ population and similar stringent limits are produced in the LTE level-population limit with $T = 9,000 \text{ K}$. LRDs are often reddened, likely at least partly due to dust, but this measurement shows the dust occurs outside the region probed by the dense hot gas cocoon itself.

Having probed the importance of bound-free opacity from $n = 3$, it is worth noting that this also implies that Paschen jumps should be observed. To our knowledge, this has not previously been observationally claimed and it is often difficult to assess given the high-redshift nature of LRDs and the observational requirement for continuum flux redward of restframe $1 \mu\text{m}$. However, we note that fitting the continuum redward and blueward of the Paschen break for lower-redshift LRDs can provide distinct continua. Finally, Balmer jumps can also be produced but the Paschen jump is more robust in the models and more distinguishable observationally, given the effects of dust reddening and blue contamination from stellar emission. While Balmer jumps are by definition not associated with the LRD population as currently defined, it has been a notable feature for a subset of high-redshift galaxies (102, 103). Our work suggests that these objects may also be LRD-like objects. We defer more detailed investigation of these findings to later work.

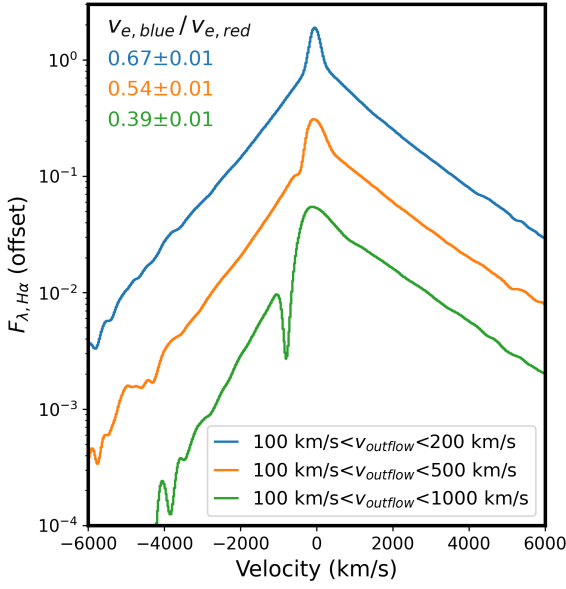


Fig. C1: Line shapes for a spherical electron-scattering medium at various wind velocities. At velocities of ~ 500 km/s, the asymmetry between the blue and red exponential wings is dramatic. To self-consistently produce both symmetric scattering and the P Cygni profiles, we must go beyond spherical models.

C Asymmetry in the exponential line-wings

In this appendix, we explore the degree of line asymmetry produced by the electron-scattering medium. For velocities of a few hundred km/s, the asymmetry should be substantial (see Fig. C1), which is in strong tension with the almost symmetrical broad lines observed (see Fig. 5). Since the majority of observed LRDs are consistent with symmetric profiles, it is worth quantifying how fine-tuned this radiative-transfer condition is; this motivation also led us to search for observational candidates that are measurably asymmetric in the line shape, such as ‘the Cliff’ (Fig. C2). We quantify here the deviations from exponential symmetry given the cocoon’s inflow/outflow structure and find that near-exponential symmetry follows for comparable mass flux in outflows and inflows. We further consider alternate interpretations of the observed symmetry due to i) low metallicities, $Z \lesssim 10^{-3} Z_{\odot}$, that reduce cooling and maintain higher electron temperatures or ii) multiple velocity components at different radii, which can produce scattering- and absorption-dominated features, respectively.

Electron scattering in a stationary medium produces a symmetric line profile (104), while outflowing environments yield asymmetric profiles with a steeper decline on the blue side for modest velocities ~ 50 km/s. This effect is seen in the spectra of symbiotic stars (105), Wolf–Rayet stars (106), tidal disruption events (107, 108), luminous blue variables (109), luminous red novae, and Type II-n supernovae (110, 111).⁴ In such systems the systematic redward skew of the line center arises from the net divergent outflow: when photons scatter into non-radial directions, the bulk velocity component away from the source imparts a net redshift (97).

⁴Symmetric exponentials have also been observed for Type II-P SNe, but these are associated with narrow intrinsic lines in low-velocity winds; e.g. SN 1998S and SN 2010jl (112, 113).

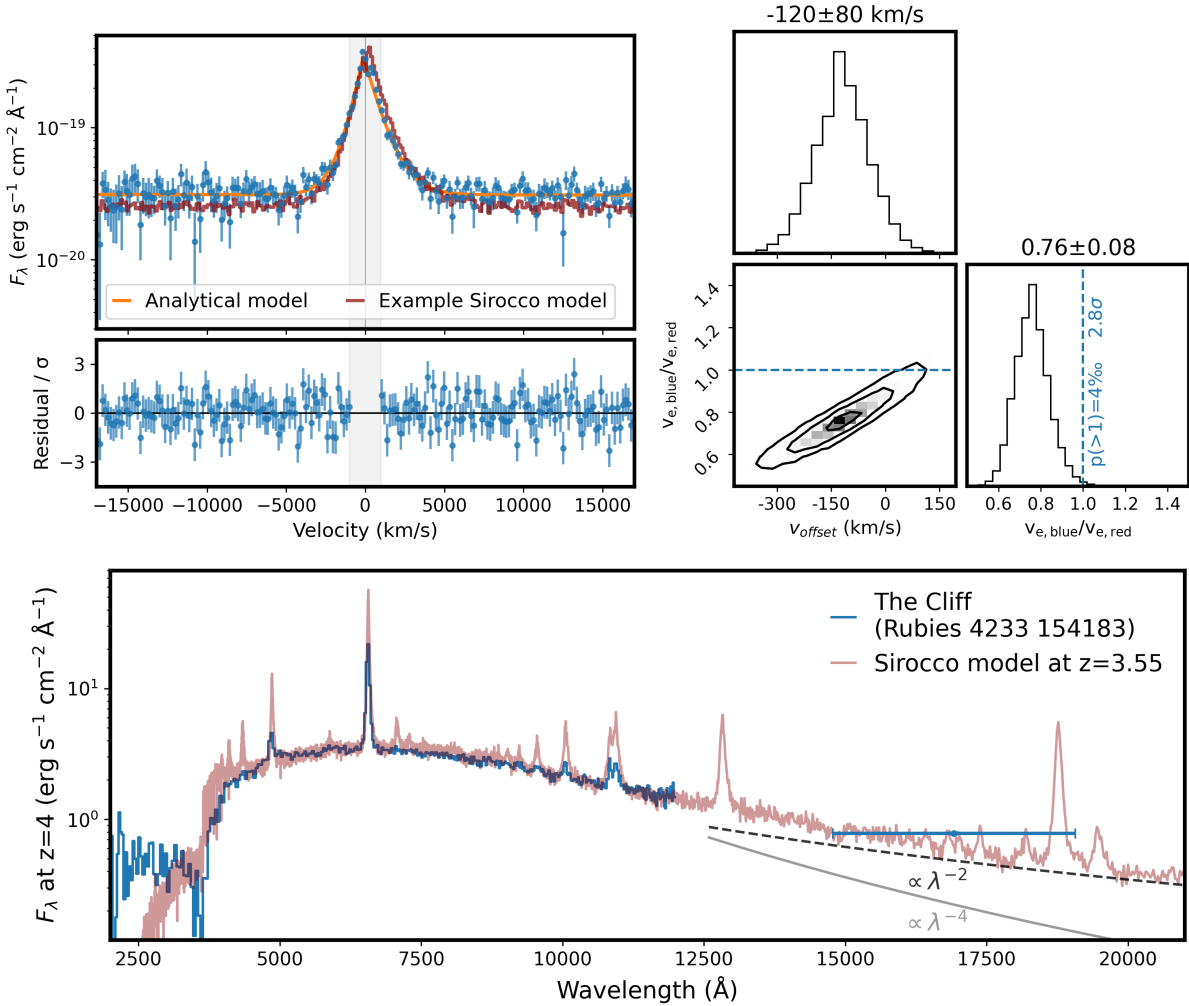


Fig. C2: The Cliff spectrum and H α line, showing clear asymmetry in the line shape. An example model using Sirocco that is a reasonable match (to the observed H α line) is also shown. *Upper left*: H α profile with continuum and electron scattering wings fit using only velocities outside the central ± 1000 km/s (orange curve). The red curve shows an illustrative Sirocco-model spectrum chosen to have a similar line-profile. *Upper right*: Posterior probability distribution for the velocity offset of the central wavelength of the broad component and the line-asymmetry parameter, showing 1, 2, and 3 σ contours. Even allowing for a shift in the central wavelength, a fully symmetric line shape is disfavoured at 2.8 σ . *Bottom*: The SED of ‘The Cliff’ and the aforementioned Sirocco-model spectra, showing that a model optimised for Balmer line-shape provides a broadly consistent Balmer break strength.

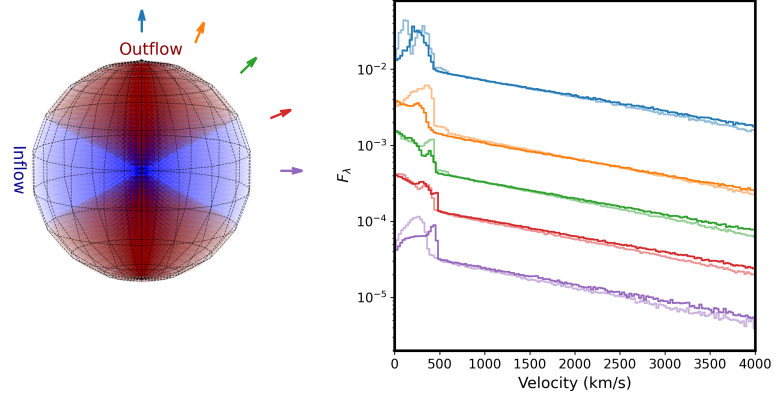


Fig. C3: Velocity distribution of a cocoon with polar outflows and equatorial inflows with equal solid angle coverage (*left*). The arrows indicate various observer directions, at 0° , 22.5° , 45° , 67.5° , and 90° from the polar axis. The corresponding Sirocco line profiles produced at these viewing angles are shown at *right*, with blue (lighter) and red (darker) wings overlaid. These lines are highly symmetric from all viewing angles ($R_{\text{in}} = 10^{15}$ cm, $100 \text{ km/s} < v_{\text{outflow}} < 500 \text{ km/s}$, $\tau_{e^-} \sim 1$). The central part of the emission is line-of-sight dependent, while the scattering-broadened line is a property of the averaged kinematics of the electrons responsible for scattering in the cocoon.

Thus, outflows tilt the profile redward (i.e. a steeper blue exponential), whereas inflows tilt it blueward (i.e. a steeper red exponential).

Parameterizing the blue and red wings with separate characteristic velocities,

$$F(v) = \begin{cases} F_0 \exp(-|v|/v_{e,\text{blue}}), & v < 0, \\ F_0 \exp(-|v|/v_{e,\text{red}}), & v > 0, \end{cases}$$

we see $v_{e,\text{blue}}/v_{e,\text{red}} \simeq 1$ to within 10% in our sample, with uncertainties for individual object at the 5% level. In one-dimensional models, this near-equality would imply that the bulk flow speed is small compared to the electron thermal speed, $v_{\text{bulk}} \lesssim 0.1 \sqrt{2kT_e/m_e} = 50 \text{ km/s} (T/10^4 \text{ K})^{1/2}$. The simplest explanation of both symmetric exponentials and high observed absorption line velocities requires a departure from spherically symmetric kinematics.

Blueshifted absorption features probe velocity outflows *along the line-of-sight*, while the asymmetry of the exponentials measures *the net kinematics* of the scattering gas as a whole. If the cocoon were a single monotonic outflow (i.e. a positive velocity divergence everywhere), an observable red-blue asymmetry would be unavoidable. By contrast, if inflows and outflows with comparable momentum coexist, their positive and negative divergences can partially cancel, yielding nearly symmetric wings. Simultaneous inflows and outflows would not be surprising in an accreting SMBH scenario of course, where the AGN luminosity arises from accretion, thus requiring an inflow, and feedback must produce an outflow.

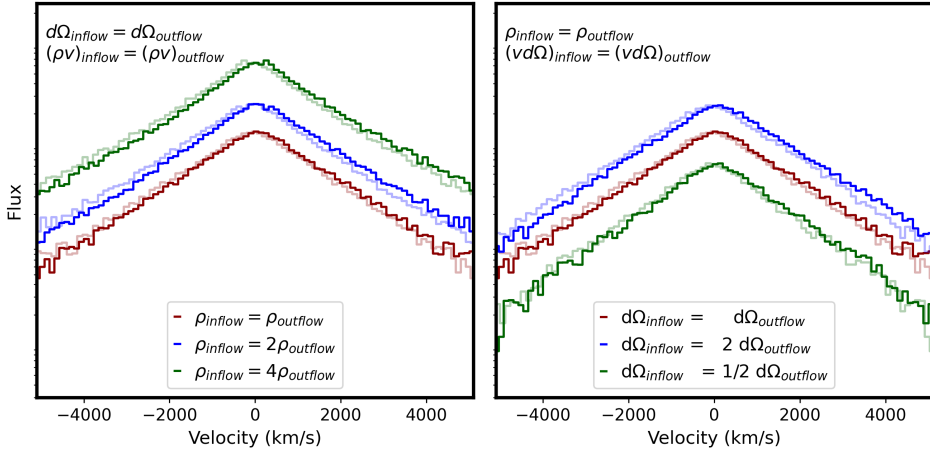


Fig. C4: Exponential-scattering wings of H α with parameters like Fig. C3, but with a variety of densities (*left*), solid angles (*right*) and velocities (*both*). Here we show the line-profile of scattered photons as well as the mirrored profile (in lighter shading), to emphasise the symmetry in these model spectra. The common constraint on all model spectra shown here is that the effective momentum of polar and equatorial components are equal. These model spectra are all consistent with symmetry at the level of the observations (i.e. $\sim 5\%$).

C.1 Deviations from symmetry

The relative contributions of the inflowing and outflowing gas to the exponential wings scales with the number of scatterings (i.e. with the electron column density), while the degree of asymmetry is dictated by the bulk velocity. Consequently, comparable mass-flux inflows and outflows naturally produce symmetric wings. The setup illustrated in Fig. C3 shows gives highly symmetric wings from all viewing angles when the inflow and outflow components have identical densities, absolute velocities, and covered solid angles. However, the inflow velocities could reasonably be expected to be much lower than the outflow velocities, as is often the case in accreting systems (114, 115). This more general case is addressed in Fig. C4, where we explore different velocities and densities (left panel) and solid angles (right panel) under the constraint that the net momentum in inflows and outflows is identical. The exponential profiles produced by Sirocco with comparable momentum in the inflows and outflows (see Fig. C4) are symmetric to within $\sim 5\%$, similar to the observational constraints of the typical LRD population, despite differences in the velocity or density. Conversely, non-mass-flux conserving flows easily produce asymmetries at levels $\gtrsim 10\%$. From these models, and the observed near-symmetry of the broad lines in most cases, we can infer that the mass fluxes in LRD-like objects must be similar in the inflows and outflows.

If the inflow becomes sufficiently dense/optically thick then photons penetrate these regions less, and the resulting scattering profile becomes increasingly dominated by the outflow region. In particular, electron-scattering wings in TDEs are dominated by the outflows and therefore

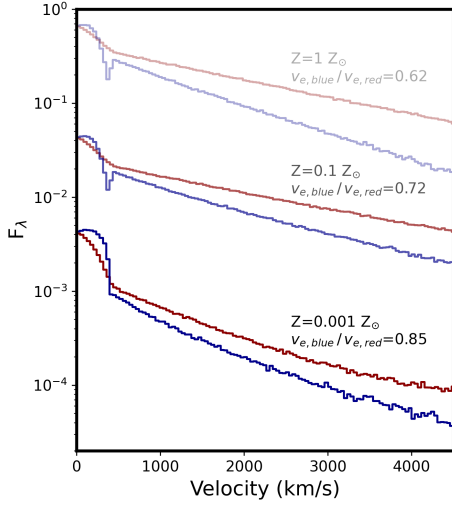


Fig. C5: The effect of metallicity on the line shapes. Here we show red/blue electron-scattered line shapes for a spherically kinematic electron-scattering medium at different metallicities. Metallicity affects the cooling, so that lower metallicities result in higher equilibrium temperatures and thus more symmetric profiles because the optical depth is lower for the same line width.

do not maintain symmetric exponential-wings (107, 108). Thus, for sufficiently high SNR data and/or for extremely dense cocoons, the differences between inflows and outflows should cause asymmetries to emerge. Indeed, as mentioned above, significant asymmetry is detected in the LRD with the strongest Balmer break, the Cliff) and in the highest SNR objects in the sample (i.e. Glimpse 17775 and GDN 14).

C.2 Alternate origins of symmetry

Alternate interpretations of the observed highly symmetric exponentials could be due to radially separated kinematic components, where the observed absorption line gas does not have the same kinematics as the scattering gas, or extremely high temperature gas, which would wash out kinematic information. First, piecewise velocity components at different radii can fit many observed line profiles. However, because the electron-scattering and Balmer-absorption regions occur on similar spatial scales, it is difficult via radiative acceleration to produce an order-of-magnitude increase in the characteristic velocity between them. If (i) the accretion process is stochastic and (ii) the duty cycle is comparable to the timescale separating the layers probed by absorption and scattering, these layers could probe different phases of activity. However, this would require fine-tuning for the LRD population as a whole, since the electron-scattering medium is generally stationary. Second, the high-temperature hypothesis is testable by asking whether the cocoon can sustain the required temperatures at LRD luminosities and plausible metallicities. This can be achieved in Sirocco with high luminosities $L \gtrsim 5 \cdot 10^{45}$ erg/s and low metallicities $Z \lesssim 0.01 Z_\odot$. However, across the LRD population with luminosities $L_{bol} \sim 10^{43} - 10^{45}$ (116), highly symmetric exponentials cannot be achieved for any metallicity (see Fig. C5). Moreover, for a given observed wing width, higher T_e implies a smaller required Thomson optical depth; in turn, photons should predominantly escape without scattering, which is generally inconsistent with the LRD population. So we can rule out this explanation.